



Laboratory acousto-mechanical study into moisture-induced changes of elastic properties in intact granite

Rui Wu^{a,b,*}, Paul Antony Selvadurai^c, Ying Li^{d,b}, Yongyang Sun^e, Kerry Leith^b, Simon Loew^b

^a State Key Laboratory of Intelligent Coal Mining and Strata Control, China Coal Research Institute, Beijing, China

^b Department of Earth Sciences, ETH Zürich, Zürich, Switzerland

^c Swiss Seismological Service, ETH Zürich, Zürich, Switzerland

^d Department of Civil and Transportation Engineering, Hebei University of Technology, Tianjin, China

^e Department of Exploration Geophysics, Curtin University, Perth, Australia

ARTICLE INFO

Keywords:

Water imbibition
Granite
Ultrasonic monitoring
Elasticity
Nanopore

ABSTRACT

The water adsorption into pore spaces in brittle rocks affects wave velocity and transmitted amplitude of elastic waves. Experimental and theoretical studies have been performed to characterize moisture-induced elastodynamic variations due to macroporous effects; however, little attention has been paid to the manner in which wetting of nanopores affects elastic wave transmission. In this work, we extend our understanding of moisture-induced elastic changes in a microcracked nanopore-dominated medium where 80 % of the surface area exhibits pore diameters (also include microcrack widths) below 10 nm. We study acousto-mechanical response resulting from a gradual wetting on a free-standing intact Herrnholz granite specimen over 98 h using time-lapse ultrasonic and digital imaging techniques. Linkages between ultrasonic attributes and adsorption-induced stress/strain are established during the approach of the wetting front. We find that Gassmann theory, previously validated in channel-like nanoporous media, does not work properly in predicting the P-wave velocity increase of microcracked nanopore-dominated media at ultrasonic frequency. However, squirt flow – a theory recognized to characterize wave velocity increase and attenuation in microcracked macropore-dominated media at the pore scale – also accounts for the observed increase of P-wave velocity in microcracked nanopore-dominated media. The transmitted amplitude changes in direct P waves are explained and predicted by the elastic wave propagation within P-wave first Fresnel zone and reflection/refraction on the wetting front.

1. Introduction

In the earth's crust, fluids can alter the material properties from near-surface to subsurface in various ways. Natural (e.g. precipitation, dew, fog, melting snow) or anthropogenic hydraulic activities (e.g. water injection, hydrocarbon production) can increase the moisture content of porous medium driven by capillary pressure, gravity and injection pressure differences. During wetting, water molecules are initially adsorbed onto grain boundaries followed by capillary condensation; liquids gradually fill, and (almost) fully saturate the interconnected pore space.^{1,2} This process induces changes in elastic properties; these have been reported in numerous *in situ* observations, varying from near-surface natural hazards, e.g. landslides related to groundwater movement or rainfall,^{3–5} engineering structure stability, e.g. thin sheet collapse of borehole/tunneling wall,⁶ building material deterioration due to fluctuating humidity⁷; and subsurface geo-energy applications involving with water flooding, e.g. oil and gas recovery, geothermal energy extraction.⁸ Observed moisture-induced elastic

variation almost always changes the propagation of elastic waves in host materials. Characterization of moisture-induced variation of elastic properties, using the theory of elastic wave propagation, plays a central role in rock-physics research.^{9,10}

1.1. Background on elastic response of porous media during water imbibition

The study of the dynamic elastic response of porous media to water imbibition has been reported from numerous laboratory and analytical studies performed on dry and saturated rocks over the past 70 years.^{10–20} High-frequency elastic waves (usually tens of kHz to MHz for laboratory measurements) are produced by ultrasonic piezoelectric transmitters and are then detected by ultrasonic receivers, which use the amplitude and wave velocity information to estimate their sensitivity to the presence of pore fluid. There is a large compendium of research on the underlying mechanisms of elastic changes due to

* Corresponding author at: Department of Earth Sciences, ETH Zürich, Zürich, Switzerland.

E-mail address: rui.wu@erdw.ethz.ch (R. Wu).

moisture ingress into macroscopic pores; however, little attention has been paid to nanopores with pore widths below 100 nm defined by Ref. 21. This gap in the experimental understanding to explain the differences between wave propagation in macropore- and nanopore-dominated media leads to this study.

In laboratory ultrasonic tests, the P-wave velocity is widely observed to increase when macroporous, clay-deficient rocks become (almost) fully saturated with water. This P-wave velocity increase, under zero confining pressure, has been reported in sandstone as 8 to 73 %^{22–26}; granite as 8 to 27%^{9,12,24}; limestone as 0 to 73%^{12,24,27} and dolomite as 28%.¹² Various physical mechanisms have been proposed to predict such P-wave velocity increase; for example, Gassmann's equation,¹¹ Biot's theory²⁸ and the squirt flow model.^{20,25} An extensive review of these models is given.²⁹

P-wave modulus changes are accurately modeled in Vycor glass³⁰ saturated by n-hexane³¹ and argon³² within the framework of classical Gassmann theory.^{11,33} Vycor glass in their study is a well-defined nanoporous medium characterized with channel-like pores with a peak throat size of around 7 to 8 nm.³⁴ However, when studying P-wave velocity increase in natural nanoporous media, such as rocks, the microstructural differences between e.g. man-made Vycor glass should not be ignored. Microcrack-based microstructures in rocks contribute to the bulk elastic changes more than round pores under varying confining pressure³⁵ or with the addition of pore fluid.³⁶ It is premature to extend the validity of Gassmann theory to nanopores in microcracked media due to the added complexities of microcracks not present in the man-made Vycor glass.^{30,37} To the authors' knowledge, there are no classical theories (e.g. Gassmann theory) relevant to materials that contain both nanopores and microcracks. As almost all natural rocks contain a full range of pore sizes, understanding such material is fundamental to earth science research.

The amplitude decay of transmitted ultrasonic waves has been linked to the elastic properties of porous media¹⁵ and it is more sensitive than wave velocity to increases in the moisture content. Laboratory earlier studies of ultrasonic monitoring showed that observed losses in transmitted amplitude were an order of magnitude larger than variations in wave velocity when the dry specimen was saturated.^{13,38} To study ultrasonic amplitude changes to the movement of wetting front, researchers^{39–43} performed water imbibition tests by submerging part of the macroporous rock specimen into a water tank below. The wetting front was driven by capillary force, where free water first wets or saturates compliant microcracks at the grain scale. They pre-installed the transmitter–receiver pairs on the specimen surface and analyzed ultrasonic signature changes with the movement of the fluid front through time. They found a significant decrease in the transmitted wave amplitude even before the entire specimen was wetting. Moreover, this water imbibition process was found to be reversible by drying.³⁹ Fluid (or solvation) pressure inside the pore spaces is generated,^{1,2} which decreases the normal stress across microcracks.⁴⁴ This process also decreases contact stiffness around the grain contact⁴⁵ and friction coefficient along microcracks.¹⁵ Passage of the elastic waves causes more relative mechanical deformation along/across microcracks and induces fluid flow within microcracks at the grain scale; as a result, more transmitted wave amplitude can be decayed.^{15,16,19}

Ultrasonic-derived changes in elastic properties can be better understood if simultaneous low-frequency mechanical deformation data is available. Ultrasonic monitoring and mechanical deformation measurements have been jointly performed in macropore-dominated rocks, e.g. Bentheim sandstone⁴⁵ and Thüringer sandstone.⁴⁶ Most of the pore diameters were measured as 40 μm ⁴⁷ for Bentheim sandstone. Adsorption-induced deformation (extensional strain of the order of 10^{-4}) and elastic modulus reduction (e.g. P-wave velocity decrease of 13 to 16%) are quantified when the relative humidity (RH) was gradually increased from 13 to 97%.⁴⁵ They attributed the observed elastic weakening/softening to be the result of solvation pressure generated

in the pore space (2 to 3 MPa in Bentheim sandstone and 18 MPa in Thüringer sandstone).

Researchers⁴⁴ moved the focus from macropore- to nanopore-dominated rocks by studying Herrnholz granite, where the majority of pore diameters are below 10 nm. They gradually wet two free-standing 90 \times 65 \times 35 mm Herrnholz granite prisms using distilled water, which maintained water ingress from their upper surfaces. Using digital image correlation (DIC) techniques, they found extensional strain with magnitudes up to 4.7×10^{-4} on the front face of prisms and calculated a solvation pressure of 40 to 47 MPa. This provided the initial mechanical constraints of the “hygroscopic expansion” process in this geomaterial.

1.2. Our study

There are no studies on the acousto-mechanical response to water imbibition in media containing nanopores and microcracks with the approach of a wetting front. It is not yet clear how P-wave velocity and transmitted amplitude respond as the water is imbibed into the nanopore space. Moreover, these changes in the ultrasonic features have not been compared with adsorption-induced deformation at relatively low frequencies. To this end, we conducted time-lapse ultrasonic pulse transmission in conjunction with DIC measurements in the Herrnholz granite subject to wetting. Waveform signature changes were analyzed: P-wave velocity and transmitted amplitude. We modeled the P-wave velocity changes with complementary hydrostatic compression tests. We also analyzed changes in ultrasonic wave amplitude in direct waves during the approach of a wetting front while simultaneously monitoring the adsorption-induced deformation throughout the entire experiment.

2. Material description

The Herrnholz granite used in these tests was obtained from the eastern side of a rock quarry located in Hauzenberg, Bavaria Germany. The rock contains nanopores and microcracks and exhibits a homogeneous fine-grained structure; it has been well characterized with respect to its petrophysical and geomechanical properties in recent studies.^{44,48}

2.1. Thin section analysis

Petrographic thin section analysis of the intact specimen (35 mm \times 22 mm \times 30 \pm 5 μm) revealed a granitic mineralogical assemblage of 50% quartz, 38% feldspar, and 11% mica by area.⁴⁴ There were observed to be several types of feldspar (plagioclase, perthite, and microcline) and mica (biotite, muscovite). We assumed the properties of feldspar and mica can be represented by plagioclase and biotite, respectively. We adopted the elastic parameters of these minerals¹⁰, Table A.4.1 and estimated the effective elastic moduli from Voigt upper bound, Reuss lower bound and Hill average.^{49–51} The bulk (K_{gr}) and shear (G_{gr}) moduli from the Hill average were 49.4 and 31.1 GPa, respectively. We provided the mineral moduli and effective elastic moduli of Herrnholz granite in Table 2 of Appendix.

Crystal sizes of Herrnholz granite range from approximately 0.03 to 1 mm with an average size of 0.23 mm and a standard deviation of 0.13 mm. In the following sections, we targeted ultrasonic waves that exhibit a wavelength above around 5 mm at a frequency below 1 MHz. The minimum wavelength (5 mm) utilized in this study is one order of magnitude larger than the mean crystal size so we assumed that the scattering effect on the ultrasonic wave attenuation would be negligible.

Thin sections were dyed with a fluorescent pigment and were observed under crossed-polarized and ultraviolet light. In Fig. 1, we showed the microcrack geometry distribution. Within boxes colored purple, black, cyan, and yellow, four classes of microcracks were observed: cleavage cracks (nearly straight and parallel distribution inside a grain), grain boundary cracks, intergranular cracks (penetrating from

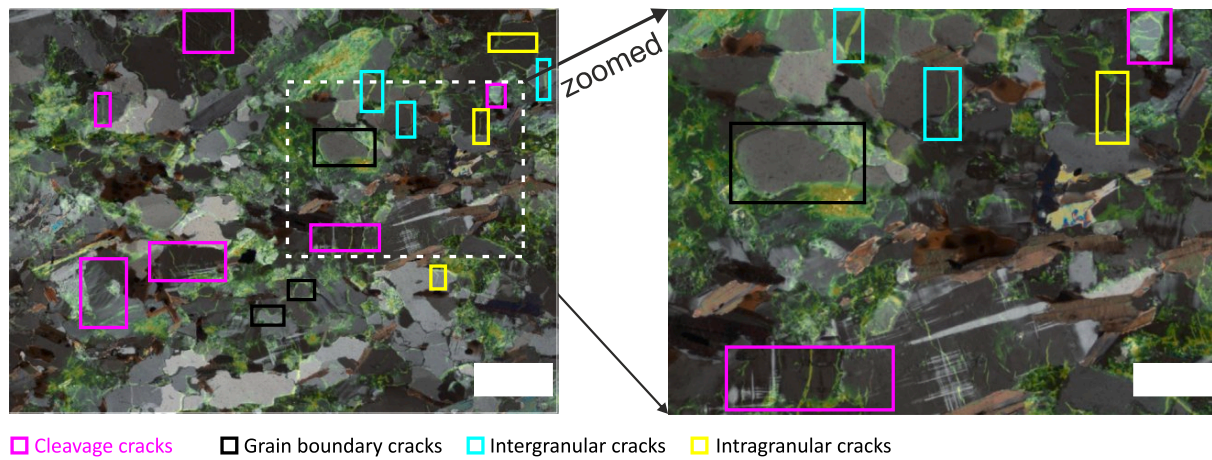


Fig. 1. Superimposed micromosaic obtained with crossed-polarized light and ultraviolet light, indicating regions of cleavage cracks (purple box), grain boundary cracks (black box), intergranular cracks (cyan box) and intragranular cracks (yellow box) (Qtz: quartz; Kf: K-feldspar; Prt: perthite; Bt: biotite; Mu: muscovite). (For interpretation of the references to color in this figure legend, the reader is referred to the web version of this article.)
Source: Reproduced with permission⁴⁴(CC BY-NC-ND 4.0).

grain boundaries to the grain inner) and intragranular cracks (random or parallel distribution inside a grain). Note that the pore size distribution results from Section 2.2 suggest that the pore diameter or crack aperture could range between around 3 to hundred nm.

2.2. Density, porosity, and pore size distribution

Density, porosity, and pore size distribution were quantified using a combination of (1) gas pycnometry, (2) mercury intrusion, (3) nitrogen adsorption, and (4) water saturation methods at ClayLab and Rock Physics and Mechanics Laboratory at ETH Zurich.

We measured the grain density (ρ_{gr}) over two prismoid specimens (dimension: 25 mm \times 25 mm \times 40 mm). These specimens were oven-dried at a temperature of 80 °C for at least 72 h. During the drying process, specimens were weighed every 24 h until variations in weight were below 0.01%. We used a helium pycnometer (model: AccuPyc II 1340) to measure their matrix volume as $22.7228 \pm 0.0118 \text{ cm}^3$ and $22.7834 \pm 0.0235 \text{ cm}^3$, respectively. Specimens were weighed as 60.526 g and 60.681 g at a precision of 0.001 g, respectively. Grain density was derived as $2.664 \pm 0.0014 \text{ g/cm}^3$ and $2.663 \pm 0.0027 \text{ g/cm}^3$. We used 2.66 g/cm^3 as the average grain density.

To acquire the bulk density (ρ_b), three granite cylinders (100 mm in length, 50 mm in diameter) were oven-dried at 80 °C following the same procedures in measuring the grain density. Bulk density was measured as the ratio of weight to volume, 2.609 g/cm^3 with an estimated uncertainty of 0.04% (or 0.001 g/cm^3). The density difference between the grain and bulk density provided us a rough estimation of total porosity (ϕ_t) of $1.9\% \pm 0.2\%$ over the granite cylinders.

To have access to the water-accessible porosity (ϕ_w), oven-dried granite cylinders were saturated by a de-airing technique⁵² lasting for 10 days. During the saturation process, specimens were kept in a vacuum chamber filled with distilled water at a vacuum pressure of 80 kPa to expel air. The specimens were weighed every 24 h by first removing the surface water using a dry cloth. The saturation process was deemed complete when a weight change below 0.01% was recorded. Water-accessible porosity was calculated to range between 1.45% and 1.53%. The estimated uncertainty was around 0.007% in the total volume of the cylinder specimen. Detailed uncertainty analysis in measuring volume, density and porosity was provided in Appendix A.

Seven specimens (20 mm \times 6.5 mm \times 6.5 mm) were prepared to measure the mercury-accessible porosity (ϕ_{Hg}) through mercury intrusion at an intrusive pressure up to 400 MPa. Mercury-accessible porosity ranged from 0.72% to 1.69% with a mean porosity of around

1.15%. The uncertainty in the mercury-accessible porosity was between 0.003% to 0.005% in the total volume of the prismoid specimen for individual measurements. Although Washburn's equation holds for the penetration of mercury through pore throats greater than around 3 nm,⁵³ intruded mercury volume was maintained when the pore diameter was lower than around 10 nm. These pores and poorly connected pores were not open to mercury even up to 400 MPa. These pore volumes were not counted into the mercury-accessible porosity (conservative estimation of the realistic pore volumes) and were assumed to contribute to the difference among the total, water-accessible and mercury-accessible porosity.

To quantify the pore size distribution below 10 nm, researchers⁴⁸ conducted the porosimetry of nitrogen adsorption over two specimens (40 mm \times 10.5 mm \times 10.5 mm) and revealed that around 80% of the surface area of this granite exhibited pore diameter below 10 nm. More discussion on porosimetry results (Figs. 12 and 13) and uncertainty analysis through mercury intrusion and nitrogen adsorption were provided in Appendix B.

2.3. Ambient P-wave velocity measurement

A suite of characterization tests was performed to quantify the P-wave velocity structure of our Herrnholz granite. We performed 3D ultrasonic tomography⁵⁴ on three cuboidal specimens of granite with a side length of 160 mm under ambient conditions. Detailed experimental setup, measurement methodology, and visualization of the P-wave velocity structure are provided in Appendix C. P-wave velocity structure and the P-wave velocity in each orthogonal direction were experimentally characterized and uniform, with $3981 (\pm 69)$, $3977 (\pm 60)$, and $3988 (\pm 64) \text{ m/s}$. The estimated uncertainty was 1.72%, 1.53% and 1.60%, respectively. To avoid specimen variability, we repeated the tests on other 2 specimens and found P-wave velocities of $3914 (\pm 74)$, $3925 (\pm 71)$, and $3982 (\pm 64) \text{ m/s}$, respectively, with an estimated uncertainty of 1.9%, 1.8% and 1.6%, respectively. We assumed the density was homogeneous throughout the specimens. We concluded that there was very weak anisotropy, heterogeneity, and specimen variability in the elastic moduli of Herrnholz granite.

2.4. Wave velocity measurement in hydrostatic compression test

We analyzed the stress dependence of the dynamic elasticity of Herrnholz granite from separate hydrostatic compression tests. Two granite, and an aluminum (model: EN AW-6082, for reference) specimens were tested under stepwise-increasing axial and confining pressure from 5 to 160 MPa. Granite specimens were prepared following the

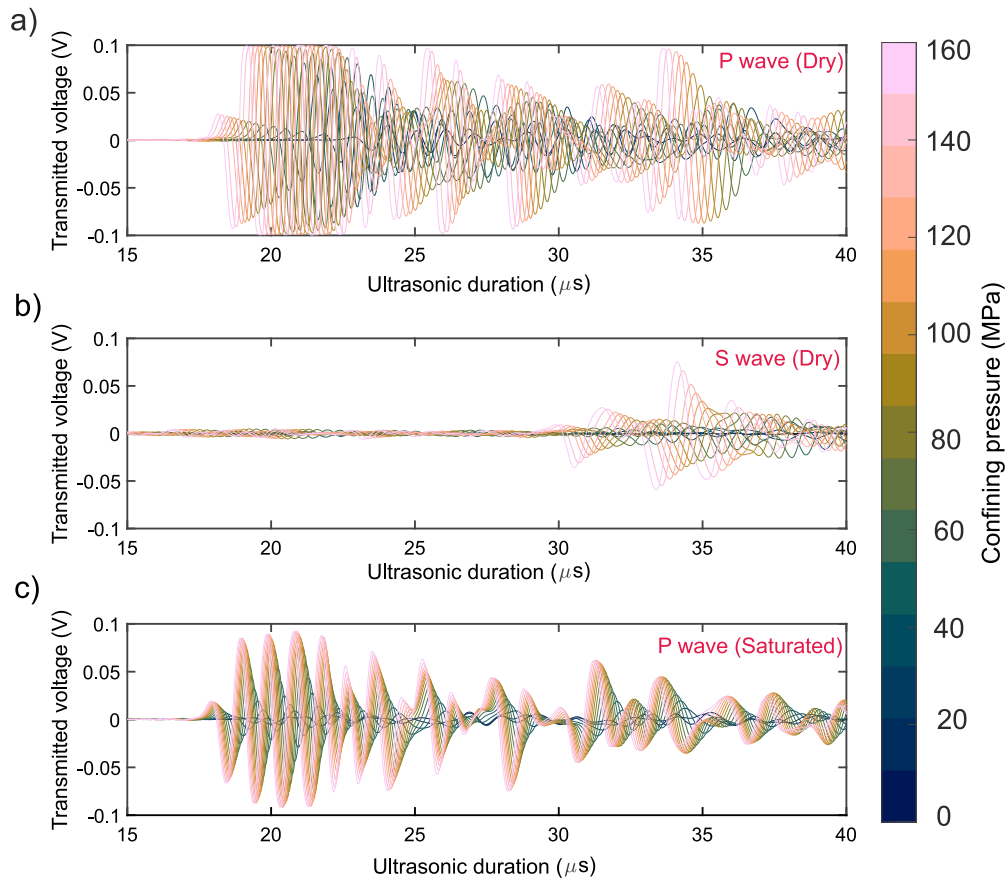


Fig. 2. Ultrasonic waveforms measured in hydrostatic compression tests over (a) dry specimen using P-wave transmitter–receiver pair; (b) dry specimen using S-wave transmitter–receiver pair; (c) saturated specimen using P-wave transmitter–receiver pair.

oven-dried (80 °C) and saturation procedures described in Section 2.2. The detailed experimental facilities and design (e.g. loading rate) were detailed in Appendix D. P- and S-wave data were acquired and digitized at a sampling rate of 50 MHz. Waveforms were stacked 4000 times for one survey; once counting 60 surveys, we stored one survey into the connected DAQ system. Their onsets of the first arrival were picked using the Aikake information criterion (AIC) technique.⁵⁵ Ultrasonic waveforms were shown between 15 to 40 μ s in Fig. 2. Triggering time was denoted by 0 μ s. Note that the ultrasonic duration was corrected from the transmit time delay for P- (8.52 μ s) and S-wave (13.32 μ s) transmitter–receiver pairs (resonant frequency around 1 MHz) provided by the manufacturer of the ultrasonic test system (Wille Geotechnik).

When confining pressure was increased from 5 to 160 MPa (color evolved from dark to pink), P-wave first arrival in the dry specimen (22.42 to 17.46 μ s) decreased much faster than the saturated case (18.86 to 17.22 μ s). We showed S waveforms measured in the dry specimen and observed higher noise before S-wave first arrival. This was because of the weak response of the S-wave transducer to the incoming P waves. We also attempted to measure S waveforms in the saturated specimen. However, we found their amplitude was strongly attenuated and almost merged into the background noise compared to the dry specimen. Meanwhile, the S-wave first motion was relatively small and usually followed by a reflection of P-wave first motion from the back of the aluminum backing piece assembled with ultrasonic transducers. We failed to pick S-wave first arrival properly. Moreover, in this study, we focused on the P-wave velocity and amplitude changes. Therefore, we did not have the S-wave velocity analysis in the saturated specimen.

The P- and S-wave velocities of the oven-dried granite specimen (red circles) increased nonlinearly with the confining pressure P_c (5 to 160 MPa) from 4450 to 5731 m/s ($\Delta V_p = 1281$ m/s) and 2736 to 3311 m/s ($\Delta V_s = 575$ m/s), as shown in Fig. 3(a) and (b), respectively.

We estimated the uncertainties in wave velocity as around 0.32% (or 18 m/s) for P waves and 0.31% (or 10 m/s) for S waves, respectively. Detailed calculation process was provided in Appendix E. Overlapped symbols denoted values from repeated pulsing tests (about 50) at each confining pressure. These gave an estimated uncertainty based on the standard deviation among repeated tests⁵⁶ and were around 12 m/s (P wave and dry), 8 m/s (S wave and dry), 2 m/s (P wave and aluminum), 15 m/s (P wave and saturated), and 1 m/s (S wave and aluminum). The P-wave velocity in the saturated granite specimen (blue squares) increased from 5271 to 5804 m/s ($\Delta V_p = 533$ m/s). Almost constant P- ($\Delta V_p = 60$ m/s) and slowly increasing S-wave ($\Delta V_s = 103$ m/s) velocities were found in the reference test of the aluminum specimen (gray crosses). Little velocity changes in aluminum could be possibly attributed to the loading system and, especially, the improved contacts between the ultrasonic transmitter–receiver pairs and the specimen.⁵⁷ No clear stress dependence of the elastic wave velocity was observed in the aluminum specimen.

2.5. Elastic piezosensitivity

We calculated the dynamic bulk (K_{dry}) and shear (G_{dry}) moduli using the expression $K_{dry} = \rho_b(V_p^2 - \frac{4}{3}V_s^2)$ and $G_{dry} = \rho_b V_s^2$ where V_p and V_s were P- and S-wave velocities of dry specimen, respectively (data from Fig. 3(a) and (b)). Bulk density (ρ_b) of the dry specimen was assumed as constant and given as 2.609 g/cm³ from previous measurements in Section 2.2. When the confining pressure increased from 5 to 160 MPa, K_{dry} and G_{dry} ranged from 26.0 to 48.2 GPa and 19.8 to 28.9 GPa, respectively (red circles in Fig. 3(c) and (d)).

We adopted a model of elastic piezosensitivity³⁵ to evaluate the effect of microcracks (porosity and aspect ratio) on the observed increase

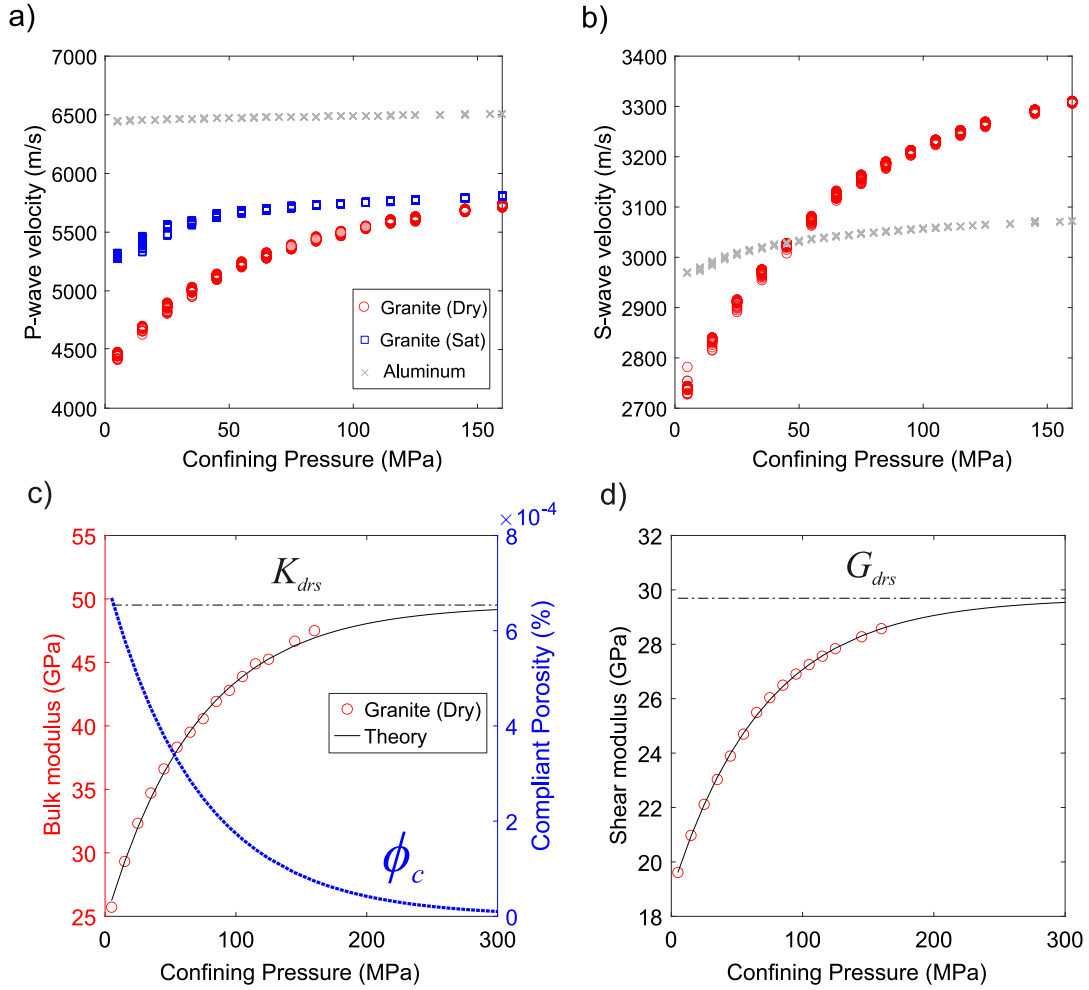


Fig. 3. Wave velocities and elastic moduli from hydrostatic compression tests. (a) P- and (b) S-wave velocity changes in Herrnholz granite (red circles) and aluminum specimen (gray crosses) in response to a series of confining pressures (5 to 160 MPa). (c) Bulk and (d) shear moduli versus confining pressure (red circles: testing data; black lines: theory). Blue dashed line represents the compliant porosity evolution. (For interpretation of the references to color in this figure legend, the reader is referred to the web version of this article.)

in the stress-dependent elastic properties. The model assumes a distribution of randomly oriented, isolated, penny-shaped microcracks in an isotropic, linear, elastic medium.⁵⁸ After reaching a confining pressure of 160 MPa, the specimen was unloaded at a stepwise-decreasing axial and confining pressure from 160 to 0 MPa. We provided the P- and S-wave velocities measured during the unloading stage in Fig. 15. We found that both P- and S-wave velocities recovered within 70 m/s and 5 m/s, respectively, of their original values. This justified our assumption of elastic conditions required in the elastic piezosensitivity model.

The elastic piezosensitivity model offers a phenomenological explanation for the observed dependency of wave velocity with confining pressure. This model assumes that increases of wave velocity are only attributed to pore and crack closure and does not consider the potential stiffening of the minerals that have been observed in other hydrostatic compression tests.^{59–61} Other models exist that estimate the crack porosity using stress dependence of elastic properties^{62–66}; however, the optimal selection of these models is outside the scope of this work and will be considered in the future.

Detailed mathematical description and parameter calculation of the Shapiro's piezosensitivity model were given in Appendix F. According to the theoretical description of K_{dry} and G_{dry} given in Eq. (11) from Appendix, we estimated the model parameters by minimizing the residual between the theories and experimental results iteratively. For penny-shaped microcracks, porosity $\phi_{c0} = 7.2 \times 10^{-4}$ without confinement and representative (average) aspect ratio $\alpha = 1.1 \times 10^{-3}$ were

derived. The bulk (K_{dry}) and shear (G_{dry}) moduli of the hypothetical granite with a closed compliant porosity were calculated as 49.5 and 29.7 GPa, respectively. Note the difference between K_{gr} and K_{dry} (or G_{gr} and G_{dry}). K_{gr} and G_{gr} are the bulk and shear moduli of mineral grain and calculated from the Hill average (see Table 2 in Appendix).

In Fig. 3(c) and (d), K_{dry} and G_{dry} (black solid line) derived from theory matched well the measured data (red circles) until 160 MPa. Above 160 MPa, theoretical solutions, extrapolated until 300 MPa, gradually approached constant values (black dashed line) which were given by K_{drs} and G_{drs} . Compliant porosity ϕ_c (blue dashed line) decreased by two orders of magnitude: 7.2×10^{-4} at 0 MPa to 1×10^{-5} at 300 MPa, which was almost completely closed. These piezosensitive parameters will be used in the modeling of P-wave velocity increase later.

3. Free-standing wetting test

The aim of the main experiment reported in this study is to understand the acousto-mechanical response in nanopore-dominated geomaterial that experiences hygroscopic expansion in response to gradual wetting. To quantify this effect, we build on the time-lapse monitoring methods of ultrasonic⁴⁵ and digital image correlation (DIC)⁴⁴ methods in the Herrnholz granite.

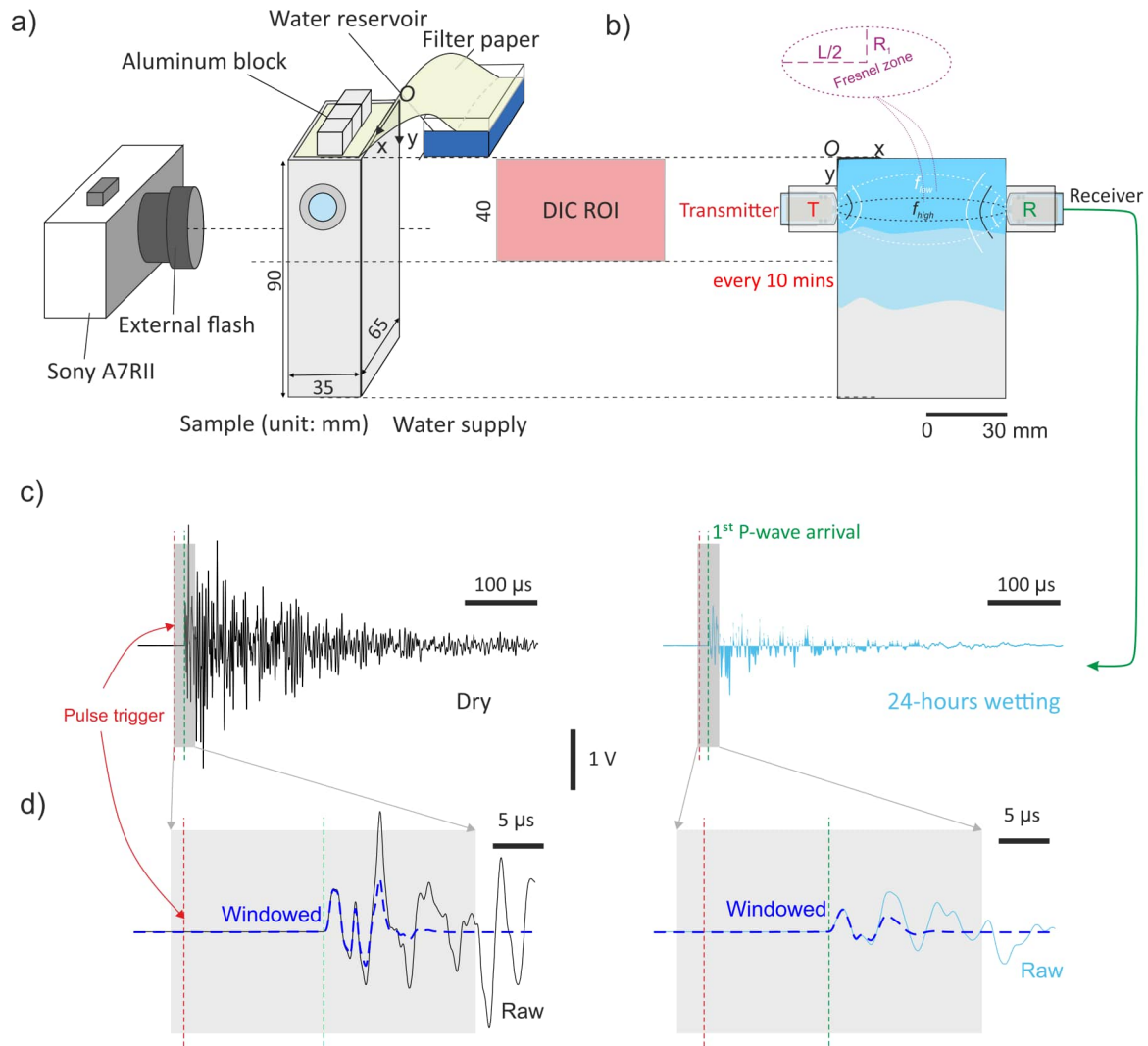


Fig. 4. Schematic diagram of the experimental setup. (a) A free-standing granite prism ($90 \times 65 \times 35$ mm) of which the upper part was subjected to gradual wetting. Mechanical moisture-induced deformation was measured on the vertical front surface in the region of interest (ROI) using digital image correlation (DIC). Figure (a) was adapted with permission from Ref. 44. (b) Ultrasonic pulsing was performed using a PZT transmitter coupled to the vertical surface 20 mm from the top of the sample. (c) Raw transmitted waveforms: dry (black) and wet (blue) measurements. (d) Windowed transmitted waveforms centered around the first P-wave arrival were used for the spectral analysis.

3.1. General setup

Water imbibition tests were performed on an intact, free-standing “prismoid” specimen of Herrnholz granite (dimension: $65 \times 35 \times 90$ mm) as shown in Fig. 4(a). The specimen was initially oven-dried at a temperature of 80°C for at least 72 h; meanwhile, it was weighed every 24 h until variations in weight were below 0.01%. Then the specimen was allowed to naturally acclimate to ambient conditions for 18 h. Water was introduced to the specimen via a filter paper that was immersed in a water reservoir (~ 15 mm above the specimen). Aluminum blocks kept the filter paper in contact with the top of the specimen and water was drawn onto the top surface by capillary forces. Distilled water was used to fill and replenish the reservoir (0, 26, 47, 71 h) over 80 h. This ensured an almost constant infiltration and imbibition of fluids into the top half of the sample that contained the region of interest (ROI) for the DIC measurements. Throughout the test, the monitored relative humidity ranged between 30 to 40%, and the temperature was kept nearly constant at 23°C . We assume that minor fluctuations in the ambient environmental conditions had negligible effects on the measured results.

3.2. Time-lapse DIC observation

A time-lapse DIC technique was utilized to measure the moisture-induced deformation on the front face of the granite specimen. In Fig. 4(a), a schematic depiction of the digital camera (model: Sony Alpha A7RII with 43.6 total megapixels) was shown; this was mounted and locked to position 240 mm from the surface of the specimen. We used the natural fine-grained granite texture as the speckle pattern, and the front surface of the specimen was imaged at a 2-minute interval and 1/13-second exposure time. A low-power Sony LED macro flash was triggered by the camera shutter in order to create consistent lighting for the images without affecting the specimen temperature.

Prior to introducing water, the specimen was allowed to equilibrate for 18 h at ambient conditions. This allowed us to evaluate the displacement and strain baselines in the absence of water. The region of interest (ROI), as shown as the pink patch in Fig. 4(b), was located 3 to 4 mm from the top and side edges to minimize boundary effect, with 58 mm in width and 40 mm in height (symmetrical about the y position of the transmitter–receiver pair). We used the open-source Ncorr software⁶⁷ to calculate the surface deformation from captured images over 98 h. This method tracks surface deformation by correlating the best fit between pixel values within a defined search window, named subset,

in a current image to those in the reference image. We set the subset radius as 50 pixels or 0.8 mm (equivalent to several crystals given the mean grain size of 0.23 mm), which on one side reduced the noise, and on the other side allowed us to track deformation at a resolution similar to the grain size. To calculate strain from the displacement field, a strain-window radius of 15 pixels (equivalent to 0.24 mm) was set. Preliminary error estimation of DIC measurements shows the mean image decorrelation coefficient is low (less than 0.1) and has little effect on the measured strain accumulation when the rock surface is progressively wetting.^{44,68}

3.3. Time-lapse ultrasonic monitoring

We adopted the pulse transmission technique^{69–71} to study changes in the ultrasonic waveform in response to water imbibition through time. In Fig. 4(b), we showed the PCT-MCX transmitter (left, red *T*) and the KRNB-PC receiver (right, green *R*) that were installed using aluminum cylinder holders at the height of $y = 20$ mm. The PCT-MCX transmitter was custom-built and its design and source characteristics were well documented.⁷² The KRNB-PC receiver was provided by KRN Services and was absolutely calibrated^{73,74} – flat instrumental response between 100 kHz to 1 MHz. Later spectral analysis is performed over this frequency bandwidth. Both transmitter and receiver followed the design of point-contact transducers to eliminate the sensor aperture effect.^{75,76} These point-contact sensors have a tip aperture diameter of 1.5 mm.

The aluminum holders were coupled directly to the sample surface using cyanoacrylate and were threaded; this allowed the ultrasonic transducers to press against the surface of the specimen with their threaded casing. For this test, a high-voltage impulse source of 500 V was applied to the PCT-MCX transmitter using the same pulsing system described in Appendix C. Pulses were emitted every 10 min over ~ 98 h. Recordings were taken around the trigger (before: 50 μ s, after: 500 μ s) to capture the wave information. Due to the more rapid transient response of the rock during the initial portions of the wetting, pulsing was performed every 2 min for 2 h after wetting commenced. Waveforms of the receiver were recorded at 20 MHz. The same DAQ system was used as in Section 2.3.

We used the Aikake information criterion (AIC)⁵⁵ to pick the onset of the P-wave arrival starting from the triggering time until 35 μ s. Triggering time was denoted by 0 μ s. This technique has been effective in laboratory ultrasonic studies.⁷⁷ We provided one example in Fig. 16 of Appendix. We picked the onset of P-wave first arrival at the location of minimum AIC value. We calculated the P-wave velocity using the ratio between specimen width ($L = 65$ mm) to the duration between the triggering time and P-wave first arrival.

3.4. Frequency-based volume of the Fresnel zone

The transmitter–receiver arrangement generated a Fresnel zone, defined as a confocal prolate ellipsoidal region between the transmitter and receiver.⁷⁸ A schematic representation was shown in Fig. 4(b) but the size of the Fresnel zone was dependent on the specimen width and the frequency bandwidth of interest. Since the Fresnel zone had an ellipsoidal geometry, we used the same nomenclature as an ellipse to describe the Fresnel zone. The elastic properties of this zone were mostly revealed by band-limited direct waves propagating along the transmitter–receiver straight ray path. The boundary of the Fresnel zone consisted of points at which the difference in the propagation distance between direct-path and deflected-path waves on the boundary was a multiple (n) of the half wavelength, $\lambda/2$. In this study, we focused on the P-wave first ($n = 1$) Fresnel zone (P-FFZ), which gave the radius R_1 of the ellipsoid minor axis as:

$$R_1 = \frac{1}{2} \sqrt{\lambda L + \frac{\lambda^2}{4}}. \quad (1)$$

Eq. (1) is only valid for a homogeneous medium. In our experiment, it provided a rough estimate of R_1 when the wetting front moved towards the bottom surface, with introduced heterogeneity around the transmitter–receiver straight ray path.

3.5. Data reduction techniques

Examples of waveforms measured under the dry (black) and wet (blue) stages showed significantly attenuated elastic waves due to water ingress in Fig. 4(c). The pulse trigger time and first P-wave arrival were denoted by red and green lines, respectively. To avoid spectral leakage and focus the analysis on the direct P-wave phase that mostly exhibits elastic changes inside P-FFZ, the waveforms were windowed using a Blackmann-Harris window centered about the onset of the first P-wave arrival. We showed details in direct waves within the gray box in Fig. 4(d). Windowed and raw waveforms were denoted by the dashed and solid lines, respectively. The window duration (e.g. gray box width) of 30 μ s (roughly twice the travel time from transmitter to receiver) was set to ensure that it would contain essential information on the direct P-wave phases and also at a satisfactory resolution of ~ 100 kHz, which was defined.⁷³

To quantify the attenuation effect, the fast Fourier transform⁷⁹ was performed to study the spectral content of transmitted amplitude from 100 kHz to 1 MHz. We calculated transmitted amplitudes as well as the noise level of waveforms shown in Fig. 4(d) and presented them in the frequency domain in Fig. 17 in Appendix. We found there was sufficient transmitted amplitude until 1 MHz compared to the noise level under dry conditions; however, transmitted amplitude close to 1 MHz under wet conditions could be not easily differentiated from the noise level. This is another reason we chose 1 MHz as the upper limit of frequency bandwidth.

We observed that waveforms acquired at sufficient wetting could merge into the noise level without signal amplification. We connected the receiver with a pre-amplifier system (Elsys AE-AMP) that allowed us to select gain settings of 0 dB, 20 dB, or 40 dB. This pre-amplifier could filter the acquired signal with a passband frequency range so that the background noise could be effectively depressed while the signal was amplified.⁸⁰ We adopted 40 dB gain to ensure extraction of the necessary message throughout the entire wetting stage.

4. Results

4.1. Moisture-induced changes in ultrasonic signatures

We analyze the changes in transmitted direct waves over 98 h (18 h under ambient conditions and 80 h of wetting). In Fig. 5(a), we show the stacked and aligned raw waveforms of 630 surveys and a visualization of the direct wave phases from –2 to 30 μ s. Ultrasonic duration is the duration offset from the pulse triggering time. An ultrasonic duration equal to 0 μ s refers to the triggering time of pulsing tests (green dashed line). A wetting time equal to 0 h denotes the time that distilled water arrived on the top surface of the specimen through the filter paper. Image color represents the magnitude of transmitted voltage ranging from –2 to 2.6 V (red: positive, blue: negative, and white: 0 value).

Transmitted amplitude is shown between the bandwidth of 100 kHz to 2 MHz in the frequency domain (Fig. 5(b)). We convert the waveform amplitude (unit: V) into amplitude (unit: dB) using $A(\text{dB}) = 20 \times \log_{10}(A(\text{V}))$. The image color indicates the magnitude of the transmitted amplitude, ranging from –45 to –8 dB (changes in the order of magnitude of 2). Summary of ultrasonic attribute changes through the gradual wetting process is provided in Table 3 of Appendix.

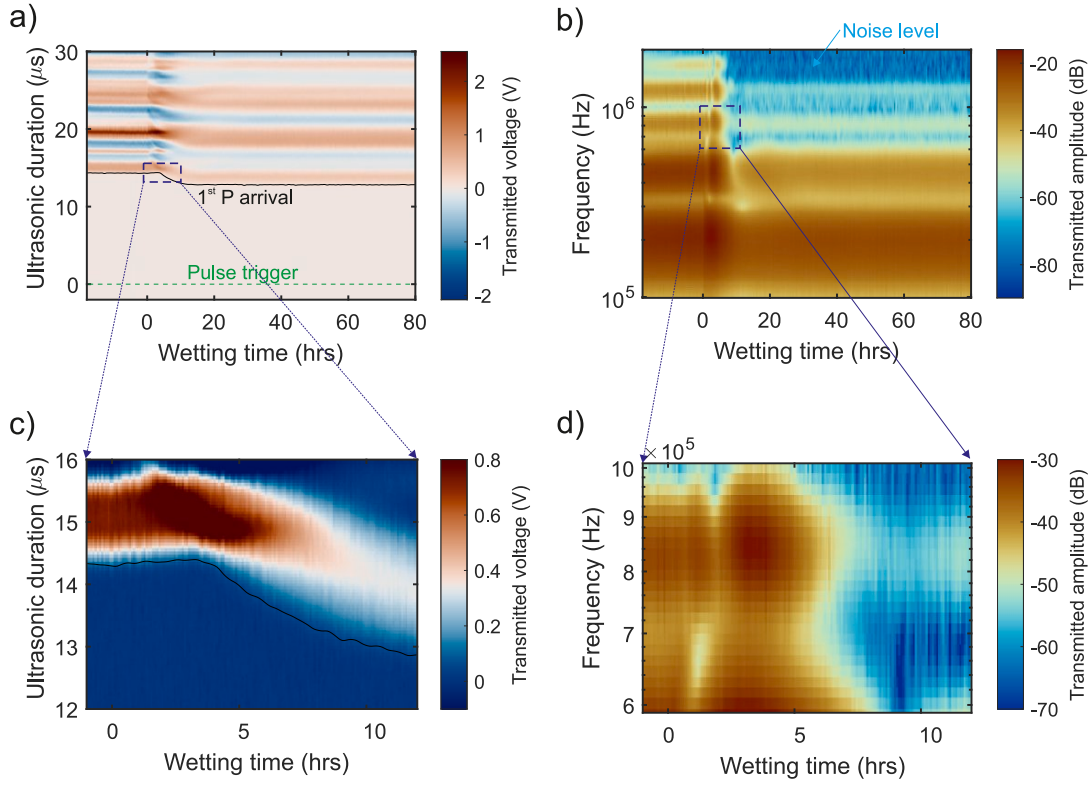


Fig. 5. Changes in stacked ultrasonic waveforms over 98 h in response to water availability. Direct waves in (a) time domain (duration: -2 to $30 \mu\text{s}$) and (b) frequency domain (frequency bandwidth: 100 kHz to 2 MHz). For details around the P-wave first arrival, direct waves are isolated between -1 to 12 h in (c) time domain (duration: 12 to $16 \mu\text{s}$) and (d) frequency domain (frequency bandwidth: 600 kHz to 1 MHz). The onset of the P-wave first arrival is shown in black and is illustrated more prominently in Fig. 6.

4.1.1. Changes in P-wave arrivals

We are interested in the changes in P-wave first arrivals upon the introduction of water and thus we isolate the results within a purple box within a wetting time of -1 to 12 h and an ultrasonic duration of 12 to $16 \mu\text{s}$ in Fig. 5(a) to Fig. 5(c). We find the onset of P waves (black line), calculated using AIC technique,⁵⁵ progressively decreases from 14.4 to $12.8 \mu\text{s}$ at an uncertainty of 50 ns between 0 to $\sim 16 \text{ h}$. Uncertainty of P-wave velocity is around 0.25% (or 13 m/s) estimated in Appendix E. In Fig. 6(a), P-wave velocity is initially measured at approximately 4538 m/s over 18 h , decreases very slightly to 4507 m/s from 0 to 3.2 h , and rises to a plateau (5074 m/s) at approximately 16 h . The onset of S waves is not included in this study because multiple reflections from the outer boundaries between the P- and S-wave onset mask the first arrival of the S waves.

4.1.2. Changes in transmitted amplitude of direct waves

In Fig. 5(c), we show the transmitted voltage between -0.1 to 0.8 V using a narrow color scale to highlight the amplitude changes around the P-wave arrival. We find the P-wave first peak is amplified (red to deep red) after the introduction of water and later attenuates (deep red towards white) to a lower value. We pick the location of the first peaks and show their amplitudes in Fig. 6(b). The amplitude maintains stable ($0.71 \pm 0.015 \text{ V}$) before 0 h , increased to $1.07 \pm 0.01 \text{ V}$ around 3.2 h , and decreases to $0.33 \pm 0.01 \text{ V}$ around 11 h followed by little recovery below 0.06 V . The amplitude maintains at $0.38 \text{ V} \pm 0.007 \text{ V}$ after 16 h .

We find that changes in the transmitted amplitude upon wetting are frequency-dependent. For example, in Fig. 5(b), there is a significant amplitude decrease (above 15 dB) above around 600 kHz and less amplitude decrease (below 5 dB) below around 300 kHz . Due to our understanding of the ultrasonic transducers, it is feasible to analyze the bandwidths over low frequency ($LF = 100$ to 300 kHz), middle frequency ($MF = 300$ to 600 kHz), and high frequency ($HF = 600$ to 1000 kHz). We isolate the results within a purple box within a wetting

time of -1 to 12 h and frequency of 600 to 1000 kHz in Fig. 5(b) to Fig. 5(d). We monitor the transmitted amplitude and find it decreases after 3 to 4 h of wetting.

We calculate the mean changes in the transmitted amplitude in dB and show them at three frequency bandwidths (LF , dashed line; MF , dotted line; and HF , solid line) in Fig. 6(c). We introduce six times from O to v which are turning points of P-wave velocity as well as the transmitted amplitude changes at HF . Time O (0 h) is marked as the thick blue line in Fig. 6. The subsequent times i (1.3 h), ii (3.2 h), iii (9 h), iv (16 h) and v (32 h) are shown as blue dashed vertical lines. Changes in the transmitted amplitude in direct waves are denoted as ΔT_d .

Prior to time O , the specimen remains in a steady state since transmitted amplitudes in direct waves are stable (all variations below 1 dB). Once water is introduced to the top surface of the specimen (time O at 0 h), ΔT_d increases from time i to ii (1.3 to 3.2 h) as the frequency bandwidth changes ($\Delta T_d^{LF} = +2.6 \text{ dB}$, $\Delta T_d^{MF} = +3 \text{ dB}$ and $\Delta T_d^{HF} = +4 \text{ dB}$). As the time increases, i.e., ii to iii (3.2 to 9 h), ΔT_d begins to decrease as the bandwidths are changed ($\Delta T_d^{LF} = -9.0 \text{ dB}$, $\Delta T_d^{MF} = -19.5 \text{ dB}$ and $\Delta T_d^{HF} = -27 \text{ dB}$). After time iii (9 h), ΔT_d starts to recover at all bandwidths ($\Delta T_d^{LF} = +0.6 \text{ dB}$, $\Delta T_d^{MF} = +5.5 \text{ dB}$ and $\Delta T_d^{HF} = +8 \text{ dB}$) and stabilizes at time iv (18 h) with a $\pm 0.1 \text{ dB}$ change over all bandwidths.

Throughout the wetting stage (0 to 80 h), the total ΔT_d at different frequencies is -4.6 dB (LF), -12.6 dB (MF), -17 dB (HF), respectively.

4.1.3. P-wave quality factor measurement

Spectral ratio method¹⁴ is utilized in this study to characterize seismic wave attenuation of Herrnholz granite independent of frequency under dry and wetting conditions. Ultrasonic monitoring of pulse transmission is performed using the same procedures that are used in the wetting experiment on Herrnholz granite specimens and a reference material, aluminum. The aluminum (model: EN AW-6060)

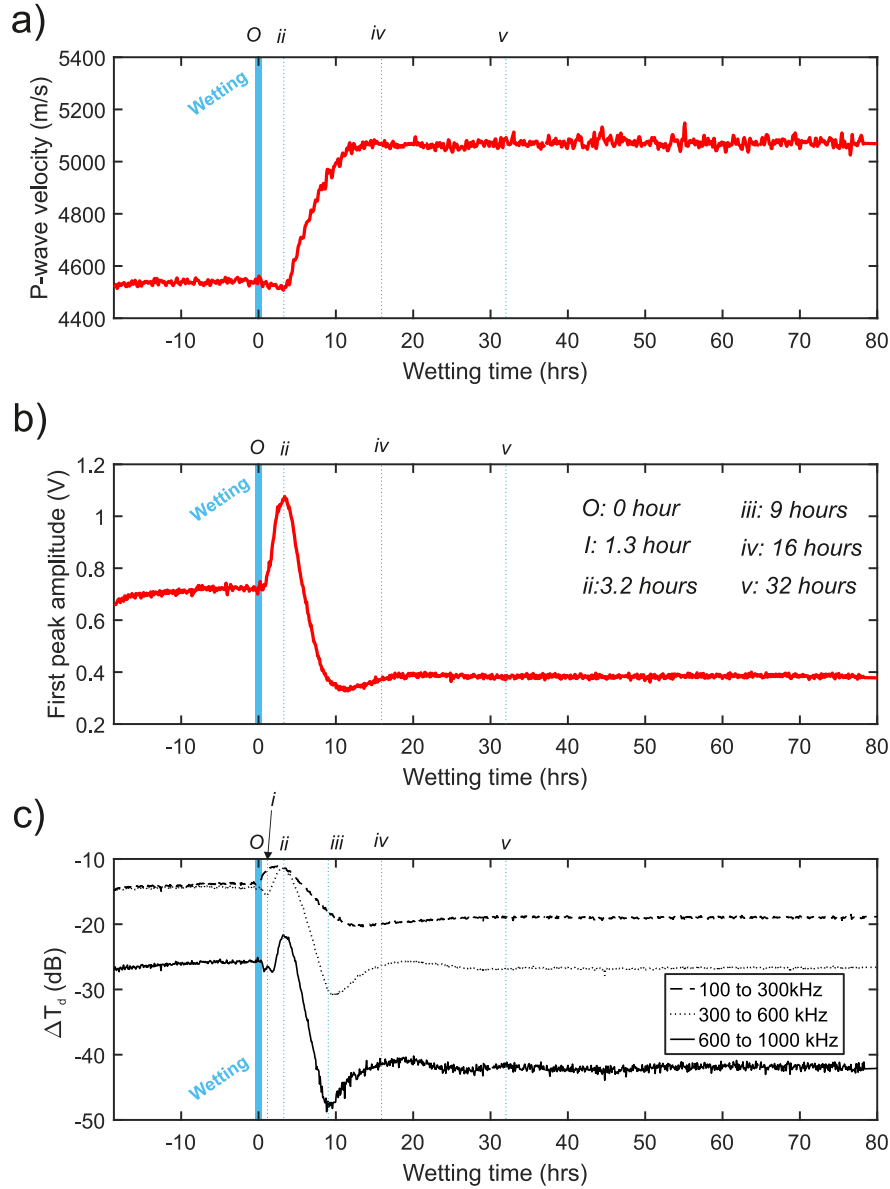


Fig. 6. Changes in ultrasonic signatures over 98 h in response to water availability. (a) Measured P-wave velocity between 4538 and 5074 m/s. Transmitted amplitude averaged at three frequency bandwidths (100 to 300 kHz, 300 to 600 kHz, and 600 to 1000 kHz) for direct waves. These frequency bandwidths are denoted as *LF*-low frequency, *MF*-medium frequency, and *HF*-high frequency, respectively. Vertical blue dashed lines indicate a few turning points of transmitted amplitude and P-wave velocity. (For interpretation of the references to color in this figure legend, the reader is referred to the web version of this article.)

is used due to its extremely low attenuation with respect to rocks.⁸¹ The geometry of the aluminum specimen is identical to the Herrnholz granite specimen shown in Fig. 4. The amplitude (A) of plane elastic body waves at the specific frequency for the aluminum (subscript 1) and Herrnholz (subscript 2) specimens can be expressed as:

$$A_1(f) = G_1(x)e^{-\frac{\pi f x}{Q_1 v_1}} e^{i(2\pi f t - k_1 x)}, \quad (2a)$$

$$A_2(f) = G_2(x)e^{-\frac{\pi f x}{Q_2 v_2}} e^{i(2\pi f t - k_2 x)}, \quad (2b)$$

where f and k are the frequency and wavenumber of the received waveforms, v is the P-wave velocity, x is the distance between transmitter and receiver (65 mm) and $G(x)$ is a frequency-independent geometrical factor that includes geometrical spreading and reflections.

Windowed waveforms of direct waves are shown in time (Fig. 7(a)) and frequency domain (Fig. 7(b)). Waveforms measured in the Herrnholz granite are aligned at the P-wave first arrival. Before the wetting stage (below 0 h), waveforms (gray line) overlap well within 18 h.

P-wave data after 27 h (light blue) remain stable until the end of the measurement. Waveforms from the aluminum specimen (dashed magenta line) are also shown and aligned at the P-wave first arrival for visualization purposes. The natural logarithm of the spectral ratio of transmitted amplitude for the Herrnholz granite to aluminum is given as:

$$\ln\left(\frac{A_1}{A_2}\right) = \left(\frac{1}{Q_1 v_1} - \frac{1}{Q_2 v_2}\right) \pi x f + \ln\left(\frac{G_1}{G_2}\right) \quad (3)$$

and is shown in Fig. 7(c). $1/Q_i$ ($i = 1, 2$) is the inverse quality factor of the direct P-wave phase. $1/Q_i$ can be simply stated as the percentage loss of carried energy in the direct P-wave phase where a high value denotes high attenuation, and vice versa. The term $\left(\frac{1}{Q_1 v_1} - \frac{1}{Q_2 v_2}\right)$ can be found from the slope of the line fitted to $\ln\left(\frac{A_1}{A_2}\right)$ because $\frac{G_1}{G_2}$ is independent of frequency. Q_1 (aluminum) is extremely high (about 1.5×10^5 by Ref. 81) compared to that for rocks (tens to hundreds) so that the term $\frac{1}{Q_1 v_1}$ is ignored. Q_2 , which represents the Q_p of Herrnholz

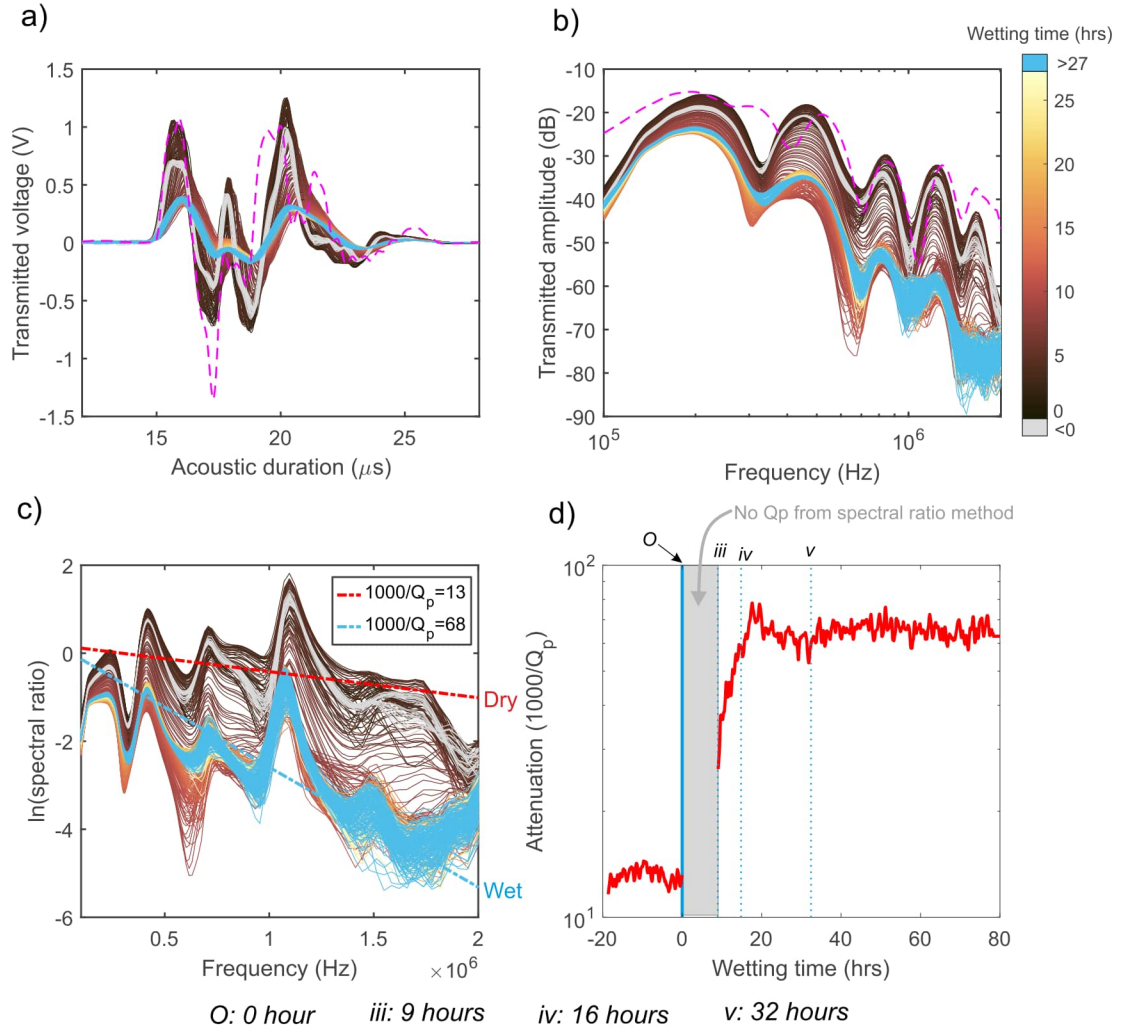


Fig. 7. Direct waves in (a) time domain and (b) frequency domain. Gray and light blue denotes the dry and equilibrium wetting stages of Herrnholz granite. Magenta represents data from the aluminum specimen. (c) Natural logarithm of the ratio of Herrnholz granite to aluminum in Fourier amplitudes. The slope is given to show how the P-wave quality factor of the granite specimen, Q_p , evolved from 87 (red dash, dry) to 16 (blue dash, wet). (d) Inverse P-wave quality factor versus wetting time (blue dashed lines indicate some turning points). (For interpretation of the references to color in this figure legend, the reader is referred to the web version of this article.)

granite, is derived using the variation in P-wave velocity as the water content increases.

In Fig. 7(d), prior to introducing water, $1000/Q_p$ remains stable (12 ± 1). We find the fitting of $1000/Q_p$ fails using the spectral ratio method from time O to iii while the rock experiences progressive wetting. It could be not possibly appropriate to use a constant $1000/Q_p$ to depict complicated changes in the transmitted amplitude at different frequencies during the progressive wetting – $1000/Q_p$ could be frequency-dependent. After time iii, $1000/Q_p$ increases by 37 up to time iv at 16 h, slowly stabilizes until time v at 32 h. After time v, few variations are observed in $1000/Q_p$ (68 ± 5).

4.2. Moisture-induced surface deformation

Using the DIC methods, 744 images are analyzed over 98 h and we observe extensional strains in both the horizontal (x) and vertical (y) directions. The vertical expansion particularly provides a useful insight into the moving wetting front. We here similarly use the contour line (1×10^{-4} , indicated by the white dashed line) of the vertical strain to track the infiltration front in Fig. 8. We present vertical strain fields from time i to v which are turnings of ultrasonic attributes previously defined in Section 4.1. We find the wetting front reach approximately

$y = \sim 9$ mm by time i or 1.3 h (Fig. 8(a)), ~ 11 mm at time ii or 3.2 h (Fig. 8(b)), ~ 17.5 mm at 7 h (Fig. 8(c)), 20.5 mm at time iii or 9 h (Fig. 8(d)), and 28 mm at time iv or 16 h (Fig. 8(e)). The vertical strain front (ϵ_{yy}) progresses past the ROI (region of interest) at time v or 32 h in Fig. 8(f); the magnitude of vertical strain is $\sim 10^{-4}$ over the entire ROI at this time. Peaks in the vertical strain field between 10 – 20×10^{-4} are observed around the upper edge of ROI and they decrease below 5×10^{-4} at $y = \sim 9$ mm. In Fig. 8(a), three dark blue patches can be observed at the top of the ROI, which corresponded to the location of the three aluminum blocks placed on the filter paper. We believe this results in a slightly heterogeneous distribution of the water on the top surface of the contact regions.

When infiltration reached 16 h, ahead of the wetting front, water vapor or a small amount of liquid water intrusion into the local heterogeneity (such as microcracks) causes extension in a few small patches (~ 10 mm \times 5 mm) with strains of ~ 0.8 to 1×10^{-4} (see Fig. 8(e)). This is also supported by the observation at 32 hours: the wetting front evolves slightly non-uniformly from left to right. The position of the ultrasonic monitoring pair is installed 20 mm below the wetting surface and the correlation between surface strain and ultrasonic changes will be discussed in Section 5.2. Results for the horizontal strain at the same six time intervals are provided in Fig. 18 of Appendix to give a tabular summary of the expansion process.

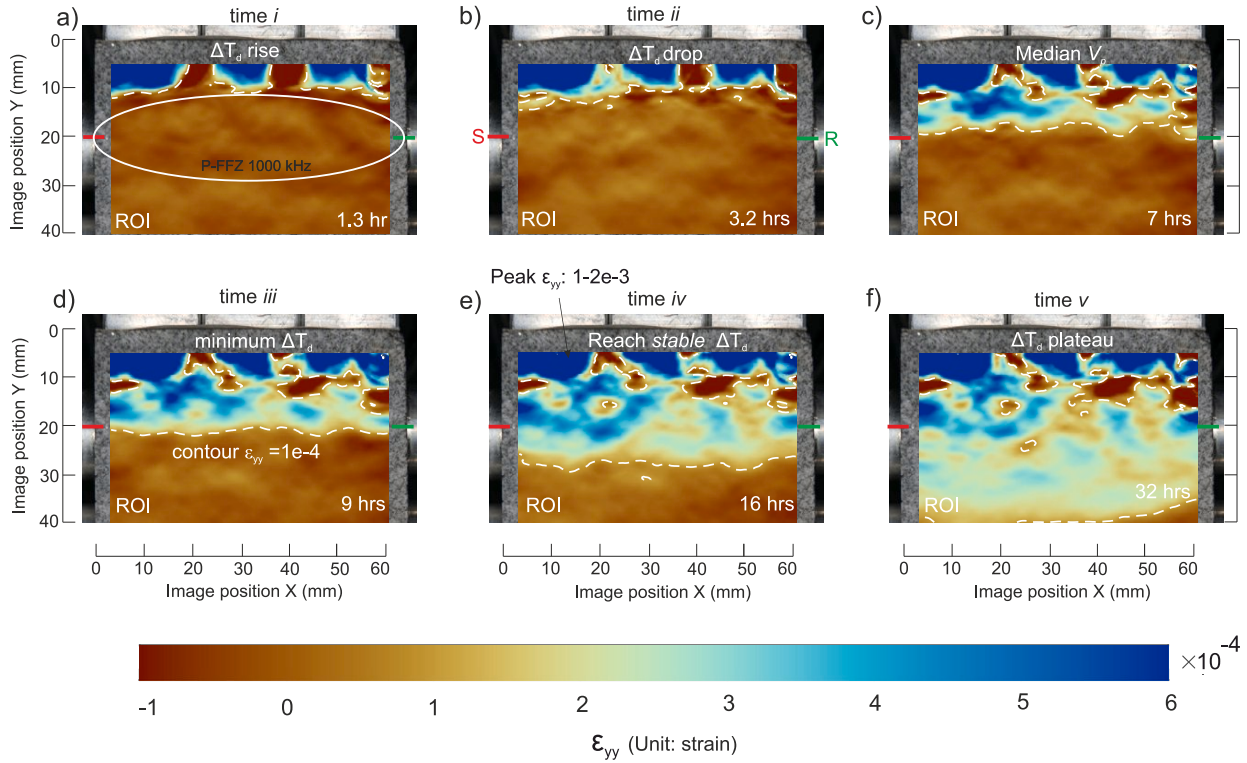


Fig. 8. Vertical strain (ϵ_{yy}) evolution on the front surface of the granite specimen (ROI: 58 mm in width and 40 mm in height) as water is applied. Wetting time equal to 0 h denotes the start of water application to the top surface of the specimen. Times *i* to *v* are the times previously defined in the ultrasonic signature analysis.

5. Discussion

5.1. Observed ΔV_p in nanopores in response to water infiltration

P-wave velocity changes, ΔV_p , observed in the free-standing progressive wetting test are discussed here. P-wave velocity increase is observed as ΔV_p increased by 520 m/s from time *ii* to *iv*. From the vertical strain evolution shown in Fig. 8(b) to (e), the wetting region is almost symmetrical around the transmitter–receiver straight ray path and overlaps with the P-wave first Fresnel zone (P-FFZ). The minor radius size of the P-FFZ, R_1 , at the frequency of 600 to 1000 kHz, ranges between 8.7 to 11.3 mm and will be discussed in Section 5.2.1. After time *iv*, the wetting front fully passes P-FFZ (Fig. 8(f)), ΔV_p stabilizes with less than a 2% variation over tens of hours. This indicates that a stable equilibrium has been reached between water wetting in the interior of the specimen and evaporation through the specimen's surfaces.

5.1.1. Squirt flow or gassmann theory in microcracked nanopore-dominated media?

We model P-wave velocity increase in saturated Herrnholt granite within the context of classic theories of fluid substitution in porous media. Gassmann theory is validated at sufficiently low frequencies (e.g. *in situ* seismic monitoring below 100 Hz and sonic logging below tens of kHz) at which fluid pressures gradients within interconnected pores, induced by elastic waves, can be dissipated within sufficient time.^{11,28} To extend the Gassmann theory to laboratory ultrasonic frequency (hundreds of kHz to few MHz), the average pore size (\bar{d}) must be much smaller than the viscous skin depth $\delta = (\eta/\pi f \rho_f)^{1/2}$.^{28,30,82} η and ρ_f represent the dynamic fluid viscosity (unit: Pa·s) and density of the saturating fluid (distilled water) (units: g/cm³), respectively, and f is the ultrasonic resonant frequency. Table 1 summarizes the essential input parameters (e.g. density, modulus, porosity, frequency) from the thin section analysis (Section 2.1), water-accessible porosity measurement (Section 2.2) and elastic piezosensitivity analysis (Section 2.5).

Table 1

Parameters for modeling P-wave velocity increase in Herrnholt granite.

Water	K_f (GPa)	ρ_f (g/cm ³)	η (Pa s)		
	2.2	1	9.4×10 ⁻⁴		
Dry rock	K_{gr} (GPa)	ρ (g/cm ³)	G_{gr} (GPa)	ϕ_s (%)	
	49.4	2.609	31.1	1.53	
Piezo	K_{drs} (GPa)	G_{drs} (GPa)	ϕ_{c0} (%)	α	f (MHz)
	49.7	29.7	0.072	1.1×10 ⁻³	1

Approximated water parameters under 23 °C and 1 standard atmosphere. Parameters in dry rocks and piezosensitivity model from thin section analysis (Section 2.1), water-accessible porosity measurement (Section 2.2), and elastic piezosensitivity analysis (Section 2.5).

We find that the assumption of Gassmann theory is satisfied⁸² because $\bar{d} = 10 \text{ nm} \ll \delta = 546 \text{ nm}$.

In Fig. 9, we further examine the applicability of the Gassmann theory to P-wave increase in intact rocks. The P-wave velocity offset between Gassmann prediction (Gass, gray) and laboratory measurement (Sat, blue) for the saturated granite specimen is greater at low effective stress (280 m/s at 5 MPa) and then decreases approaching 0 m/s, until the maximum effective stress (79 m/s at 160 MPa). By comparing the microstructural differences in nanoporous Vycor glass^{30,34} and Herrnholt granite, the effects of natural microcrack characteristics of brittle rocks might contribute to this mismatch.

Researchers²⁵ quantified the effect of compliant pore spaces or microcracks on elastic stiffening in saturated porous media. This is usually referred to the Mavko-Jizba squirt flow theory. The entire pore space is partitioned into a few subsets of stiff and compliant spaces. Compliant pore spaces are presumed to be thin cracks and grain contacts. At sufficiently high effective stress, most of soft pore spaces can be compressed to close, or at least be substantially reduced in volume. The stiffness difference between the measurements and Gassmann theory could then be expected to be the result of the unrelaxed/undissipated pore pressure inside the microcracks that resists deformation imposed

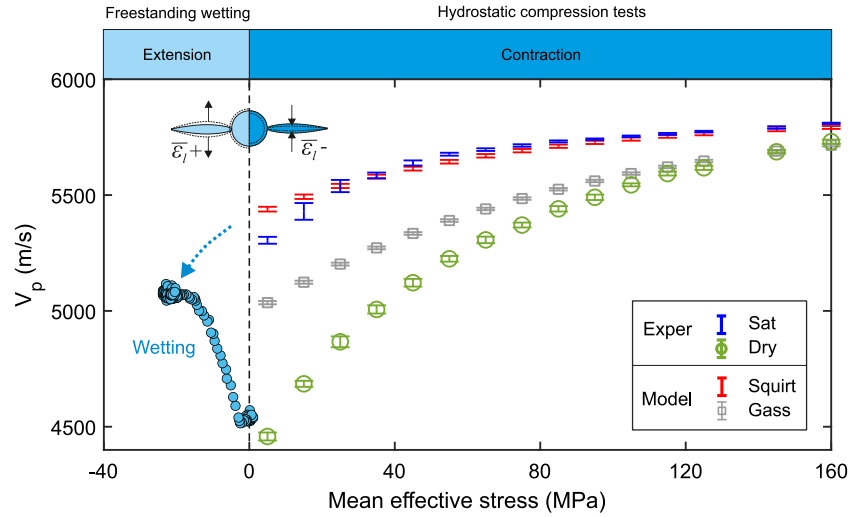


Fig. 9. Broadband V_p increase in Herrnholt granite under extensional (left) and contractional (right) stress regimes. Left: V_p evolution from dry to wet measured in the water imbibition test; Right: V_p measured and modeled in the hydrostatic compression test. dry (green, experimentally measured), Sat or saturated (blue, experimentally measured), Gass or Gassmann theory (gray, model prediction) and Sqrt or squirt flow theory (red, model prediction). (For interpretation of the references to color in this figure legend, the reader is referred to the web version of this article.)

by the passage of elastic waves. This work was extended to a broader frequency range by considering fluid pressure relaxation in penny-shaped gaps between adjacent grains.²⁰ They inferred that V_p is exactly consistent with the Gassmann theory at a low-frequency limit and transitions to the Mavko-Jizba squirt flow at a high-frequency limit. We follow their methodology and provide the detailed calculation process of V_p at all frequencies in Appendix G. Parameters for the squirt flow model used here are provided in Table 1. We roughly estimate the critical squirt flow frequency as $f_c = \frac{K_{gr}\alpha^3}{\eta} \approx 70$ kHz.¹⁰ Above f_c , the squirt flow theory should work but needs further validation.

To test the validity of the squirt flow model, we compare the predicted V_p from the squirt flow model (Sqrt, red) and laboratory measurement (Sat, blue) at 1 MHz for the saturated granite specimen in Fig. 9. In general, the error is less than 0.8% of measured V_p indicating this model is capturing the observed physics. An anomalous V_p offset of 125 m/s between the Sqrt and Sat at 5 MPa could indicate a contact problem between the granite specimen and adjacent transmitter-receiver pair at low confining pressure. As the effective stress increases, the error between observed and modeled V_p remains below 40 m/s (0.8% of measured V_p) and the V_p from squirt flow model correlates well with the V_p changes with confinement for the saturated specimen. While the Gassmann theory works well in nanoporous materials as having stiff pore spaces (e.g. Vycor glass),^{30,34} we conclude that P-wave velocity increase in water-saturated microcracked nanopore-dominated media can be better modeled using the squirt flow theory.

5.1.2. ΔV_p in granite under extensional and contractional stress regimes

After testing the validity of the squirt flow theory in the tested granite, we then study V_p increase under both extensional and contractional stress regimes. Hygroscopic expansion occurs in the water imbibition test (see Section 4.2) as is assumed to be a result of the generation of adsorption stress (also known as solvation pressure) through adhesion and capillary condensation.⁴⁴ They estimated this adsorption stress by multiplying the mean strain (denoted as $\bar{\epsilon}_l$) by the pore-load modulus M_{pl} : $\sigma_s = M_{pl}\bar{\epsilon}_l$. M_{pl} describes a linear relationship between the adsorption stress and mean strain and quantifies the deformability of porous media in response to changes in pore fluid pressure.^{30,83}

The pore-load modulus M_{pl} is assumed to be independent of the gradually wetting process controlled by hygroscopic expansion and is given as $M_{pl} = \frac{3}{1/K - 1/K_{drs}}$. K is the drained bulk modulus of the granite and is measured independently to be 18.8 GPa at 20% RH.⁴⁴

The bulk modulus of the granite without pore space, $K_{gr} = 49.4$ GPa, is determined in Section 2.5. M_{pl} is estimated to be 91 GPa and thus the solvation pressure is derived as a function of $\bar{\epsilon}_l$. The mean hygroscopic strain can be given as $\bar{\epsilon}_l = (2\epsilon_{xx} + \epsilon_{yy})/3$, where ϵ_{xx} and ϵ_{yy} are average horizontal and vertical strains within a rectangular region symmetrical around the transmitter-receiver pair.⁴⁴ The dimension of this region is 58 mm \times 20 mm. More details about this region will be discussed in Section 5.2.1.

To maintain consistency in the contractional condition, mean effective stress $\bar{\sigma}_e$ is adopted instead of solvation pressure (σ_s) by considering $\bar{\sigma}_e = -\sigma_s$ in the case of a free-standing specimen where the specimen is subjected to a zero external stress state. Changes in P-wave velocity and the calculated solvation pressure from the water imbibition test are shown as solid blue circles on the left side in Fig. 9. When the specimen saturation changes from ambient humidity conditions (around 20%) to progressively wetting, V_p and $\Delta\sigma_s$ increase by 520 m/s and 23.9 MPa, respectively. V_p at 0 MPa in the water imbibition test is slightly higher (60 m/s) than V_p at 5 MPa in the hydrostatic compression test. This slight discrepancy is because the ultrasonic monitoring requires ~ 5 MPa of confining pressure to generate a proper bond at the contact surface. The steady Wet V_p at 23.9 MPa in the water imbibition test could serve as the bound constraint of V_p in the saturated granite at the same $\bar{\sigma}_e$. Following the blue dash arrow in Fig. 9, it is possible that the changes seen in V_p between Wet and Sat V_p could be explained by that squirt flow theory. This may indicate the squirt flow theory could be also valid for extensional stress regimes, but this requires more validation work. For example, in the free-standing wetting test, rock cannot reach the full saturation status through water imbibition; however, squirt flow theory was developed on the assumption of fully saturated rocks. The observed consistency in V_p between Wet and Sat provides a straightforward understanding of P-wave velocity increase in saturated microcracked nanopore-dominated media spanning stress regimes in both contraction and extension.

5.2. Variations in transmitted amplitude due to water imbibition

Our results indicate that the squirt flow mechanism can account for P-wave velocity increase in nanopore-dominated granite, and could also be one of the major causes of seismic attenuation of passing elastic waves. In this section, changes in the transmitted amplitude of the direct P waves at high frequency are investigated and correlated with simultaneous surface deformations. We find that the transmitted

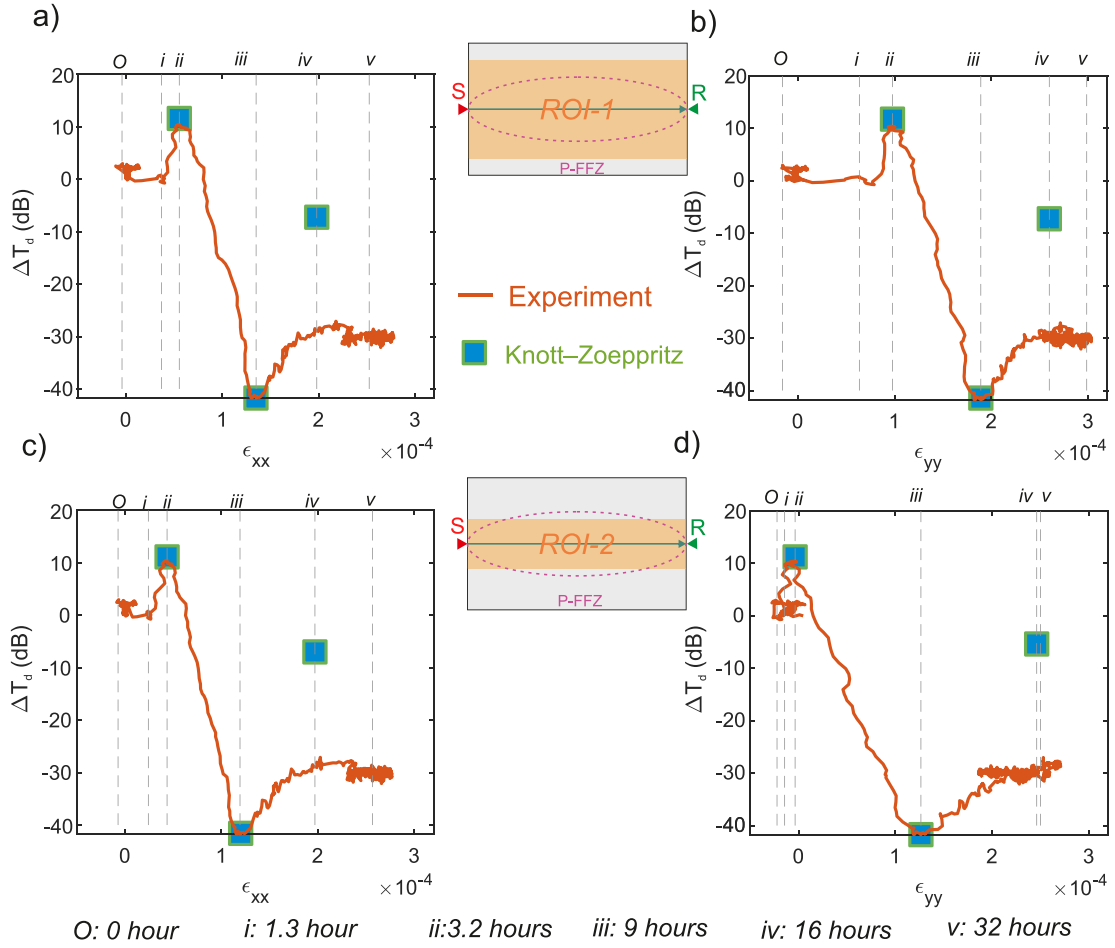


Fig. 10. Transmitted amplitude of direct waves from experimental measurement (orange solid line) and theoretical analysis (square symbol) evolution with imaged strain (left: horizontal or ϵ_{xx} , right: vertical or ϵ_{yy}). Strain is averaged within box ROI-1 for (a) and (b), and box ROI-2 for (c) and (d), respectively. Vertical gray dashed lines denote times O to v that are previously defined in the ultrasonic signature analysis. (For interpretation of the references to color in this figure legend, the reader is referred to the web version of this article.)

amplitudes at relatively high frequencies are much more sensitive to the approach of a wetting front than at low frequencies (see Fig. 6(c)). As a result, we focus attenuation on the high-frequency transmitted amplitude changes for the direct waves ΔT_d (orange solid line) between 600 to 1000 kHz, shown in Fig. 10. Imaged strain is averaged within a rectangular box ROI-1 with dimensions of 60×30 mm that is symmetrical along the transmitter–receiver straight ray path. ΔT_d and ΔT_c are correlated with imaged strain evolution (left: horizontal or ϵ_{xx} , right: vertical or ϵ_{yy}). Times O to v, delineated by the vertical dashed lines, correspond to the same times given in Section 4.1.

5.2.1. Direct P wave: ΔT_d

A peculiar observation is made with ΔT_d after the initial introduction of the water to the specimen. ΔT_d initially remains stable until time i when the wetting front is inside box ROI-1. The theoretical R_1 of P-FFZ is 11.3 mm at 600 kHz and 8.7 mm at 1000 kHz, respectively (Eq. (1)). Comparing the relative position of the wetting front and P-FFZ, the ΔT_d plateau remains because the direct P-wave phase mirrors the elastic changes within the P-FFZ. The ΔT_d plateau is followed by a small increase from 0 dB at time i to 10.4 dB at time ii. A similar increase is also observed in the P-wave amplitude (first peak) in water imbibition experiments on Sherwood sandstone (mean pore throat diameter of $18 \mu\text{m}$ ⁸⁴). Since the proposed mechanism is related to squirt flow that only accounted for seismic attenuation, there should exist another mechanism for seismic amplification.

5.2.2. Analytical solution of plane wave propagation to explain ΔT_d

We aim to provide an explanation for the increase in ΔT_d starting from elastic wave reflection and refraction between the wetting front and incident P waves in P-FFZ. We realize that the direction of the elastic wave propagation between the ultrasonic transmitter and the receiver is orthogonal to that of the moving wetting front. Thus we adopt an explanation established from a 2D plane wave propagation model⁸⁵ where the varying moisture conditions change the material properties and contribute to the presence of a distinct layer in the medium. We suggest this layer occurs at the wetting front and has properties of both the dry and wet granite across this heterogeneity. This layer is assumed to be ideally flat and sharp and represents the solid–solid interface of the wet (above) and dry (below) regions. The point transmitter and receiver are assumed to generate and receive elastic waves. For the dry phase, $\rho = 2.609 \text{ g/cm}^3$, $V_p = 4550 \text{ m/s}$ and $V_s = 2750 \text{ m/s}$. For the wetting phase, $\rho = 2.63 \text{ g/cm}^3$, $V_p = 5300 \text{ m/s}$ and $V_s = 2850 \text{ m/s}$. In Fig. 11(a), the wetting front is located above the transmitter–receiver straight ray path. Depending on the incident angle θ , incident P waves could arrive at the receiver directly along the shortest path, i.e., $\theta = 90^\circ$, along the green solid line. At $\theta < 90^\circ$, incident P waves along the green dashed line will reflect on the interface, convert into critically refracted P (denoted as Pp) and S (denoted as Ps) waves and arrive at the receiver with a time delay from the direct P waves. We adopt the same nomenclature.⁸⁵

We present the complete solution (green line) of the incident plane P-wave reflection coefficient R_p on the solid–solid interface, solved using Knott-Zoeppritz equations^{10,86,87} in Fig. 11(c). Unit conversion

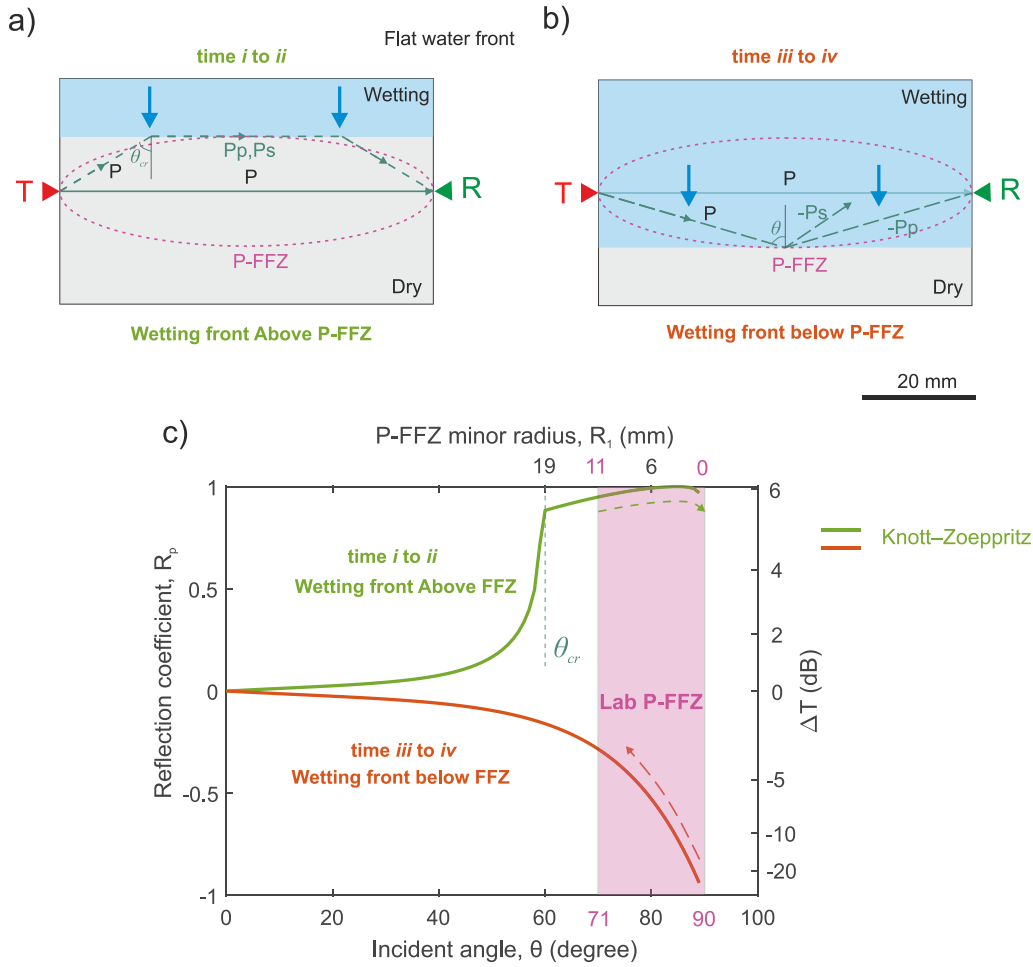


Fig. 11. Reflection and refraction of incident P waves on the wetting front. (a) Wetting front migrates from the top surface of the specimen to interact with the top co-vertex of the P-FFZ. (b) Wetting front moves from the transmitter–receiver straight ray path to the bottom co-vertex of the P-FFZ. (c) Reflection coefficient R_p in (a) and (b) by solving the Knott-Zoeppritz equation (solid lines). The pink shaded area denotes the minor radius range R_1 of the laboratory P-FFZ. (For interpretation of the references to color in this figure legend, the reader is referred to the web version of this article.)

between R_p (left y-axis) and ΔT_d (right y-axis) is given by $\Delta T_d = 20\log_{10}(1 + R_p)$. A turning point of 60° denotes the grazing angle beyond which total internal reflection occurs with R_p close to 1. When the wetting front arrives at the top co-vertex of 600 kHz P-FFZ at $R_1 \approx 11$ mm or $\theta \approx 71^\circ$, refracted P and S waves started to affect the initial direct P wave and enhanced the amplitude with synthetic waveforms. From time *i* to *ii*, the wetting front continuously moves downwards with a vertical distance away from the transmitter–receiver straight ray path from an average 11 mm to an average 9 mm. This observation matches well with the theoretical R_1 of P-FFZ, which is 11.3 mm for 600 kHz and 8.7 mm for 1000 kHz. The slight difference could be due to the definition of the dry/wet region (strain below and above 1×10^{-4}), position estimate of the non-uniform wetting front, the gap between experimental and ideal conditions (e.g. finite-dimension specimen, heterogeneity in saturation). Simultaneous monitoring of ultrasonic and DIC imaging effectively constrains the P-FFZ size which has allowed us to develop a model to better describe these observations. We conclude that from time *i* to *ii*, the wetting front continuously interacts with the P-FFZ, characterized by the frequency increasing from 600 kHz. The experimentally observed ΔT_d is enhanced by 10.4 dB, compared to the theoretical estimate of 11.6 dB shown in Fig. 11(c).

Proper correlation of transmitted amplitude changes with surface deformation requires an understanding of the physics occurring in the same region. Inconsistent variation between ΔT_d and ϵ_{xx} or ϵ_{yy} from time *O* to *i* originates from the size difference between the DIC ROI and P-FFZ. This motivates us to use another rectangular box *ROI-2*

(dimension: 60×16 mm) as the new DIC ROI where the averaged ϵ_{xx} and ϵ_{yy} within *ROI-2* are shown in Fig. 10(c) and (d). At time *O*, *i* and *ii* (with a similar finding in time *iv* and *v*) there is almost the same strain, which suggests an acceptable overlap between the DIC ROI (box) and F-PPZ (ellipse). From time *ii* to *iii*, the wetting front enters all P-FFZs between 600 to 1000 kHz. ΔT_d decreases relatively linearly with the imaged strain until the maximum attenuation of -41.6 dB is reached. At time *iii*, the wetting front slightly surpasses the position of the transmitter–receiver straight ray path and the amplitude sign of refracted P and S waves will be opposite to the direct P wave with a phase shift of 180° as shown in Fig. 11(b). No total internal reflection occurs. The theoretical estimation of ΔT_d is given as -41.8 dB at $\theta \approx 88.5^\circ$, compared to the experimental observation of -41.6 dB.

Once the wetting front passes the transmitter–receiver straight ray path, ΔT_d recovers after time *iii*. ΔT_d remains at -30 dB with 1 dB variation at time *iv* when the wetting front leaves the P-FFZ. The orange line in Fig. 11(c) is the Knott-Zoeppritz solution, and shows R_p that slowly recovers from -48 dB at $\theta \approx 89^\circ$ ($R_1 \approx 0$ mm) to -7.2 dB at $\theta \approx 71^\circ$.

The difference between experimental observations (-30 dB) and the theoretical estimations (-7.2 dB) could originate from hygroscopic expansion and squirt flow. Hygroscopic expansion due to water infiltration occurs and reaches a mean extensional strain of 2.6×10^{-4} within *ROI-2*. This induces an internal solvation pressure of 23.9 MPa. Hygroscopic expansion reduces the effective normal stress (0 to -23.9 MPa, where minus denotes extension) across the contact area of microcracks

filled with water. Less ultrasonic wave amplitude is transmitted through the weakly contacted microstructure. When elastic stress waves pass the wetting region, the microcracks are compressed, and local pressure gradients are created. We suggest the pore fluid absorbed along the microcracks will squirt into stiff pores against internal friction so that the transmitted energy is partly transformed into heat energy. It has been previously noted that the squirt flow dominates at zero effective stress and almost disappears when microcracks close^{20,25}; hygroscopic expansion can be expected to increase pore aperture, and therefore enhance the squirt flow effect, resulting in higher ΔT_d . The combined effects of squirt flow and hygroscopic expansion will decrease the ΔT_d .

Note that it is not sufficiently mature to extend the explanation for the changes in ΔT_d modeled by a two-layered medium to all other water imbibition experiments. Researchers⁸⁸ checked their ultrasonic dataset tested on 12 different rocks during the water imbibition experiments. They adopted similar assumptions⁸⁵ and calculated the reflection coefficients from Knott-Zoeppritz solution and experimental measurements. They found that although successful in 3 tests, the assumption failed in 9 tests due to the small values of the reflection coefficients from Knott-Zoeppritz solution, and the delay in arrival time of the reflected waves in the tested rocks. We realize that in our study, Knott-Zoeppritz solution is successfully applied to account for changes in ΔT_d ; however, for other scenarios, there could be other accompanying underlying mechanisms, i.e. moisture diffusion.⁸⁸

6. Conclusions

Realizing the gap in the understanding of elastic variations between macropores and nanopores in microcracked media, we quantify moisture-induced elastic changes in intact Herrnholz granite, a microcracked nanopore-dominated medium, through a laboratory time-lapse acousto-mechanical study. Changes in P-wave velocity and ultrasonic wave amplitude are examined over 98 h utilizing time-lapse ultrasonic monitoring. Simultaneous digital image correlation is performed to track the wetting front in real-time and calculate the adsorption-induced strain and stress.

At ultrasonic frequency, while the validity and applicability of Gassmann theory are confirmed in channel-like nanoporous media,³⁰ we find that Gassmann theory does not work properly in microcracked nanopore-dominated media. To bridge the gap, we verify that P-wave velocity increase in such media can be properly modeled in the framework of classical squirt flow theory, which has been validated in many microcracked macropore-dominated media. This enables the possibility of applying the mature theory in conventional rock physics to nanopore-dominated media. We also find it could be possible to extend the applicability of squirt flow theory from contractional to extensional stress regimes, which is crucial to capture the response of microcracked media to fluid substitution from deep underground to near-surface conditions. However, more validation work is required in the future.

The transmitted amplitude changes in the direct P waves are well-correlated with moisture-induced strain observed around the first Fresnel zone. Ultrasonic attributes show amplification, attenuation, and recovery in response to the approach of the wetting front. After a comprehensive study of analytical analysis and experimental observation, we conclude that these attributes behave in a predictable manner, which is assumed to be associated with the elastic wave propagation near the first Fresnel zone and reflection/refraction on the wetting front. This finding provides the ability of using elastic wave propagation to quantify elastic changes in porous media as a result of gradual wetting.

Declaration of competing interest

The authors declare that they have no known competing financial interests or personal relationships that could have appeared to influence the work reported in this paper.

Data availability

Data will be made available on request.

Acknowledgments

The authors would like to thank Elsys company, especially Roman Bertschi, for their hardware and software support for this research. The authors are indebted to Mrs. Sally Selvadurai (scientific Editor at Assist-Ed) for her thorough proofreading and editing of the manuscript. Mr. Wu and Dr. Li are financially supported by the chair, Professor Simon Loew, and the China Scholarship Council, China. This work is supported by Swiss National Science Foundation (SNSF), Switzerland R 'Equip "Long-term damage evolution in brittle rocks subject to controlled climatic conditions" (Project 170746) and "Physical constraints on natural and induced earthquakes using innovative lab-scale experiments: The LabQuake Machine" (Project 170766). Partial funding for Dr. Paul Antony Selvadurai is provided from the European Research Council (ERC) project FEAR (Grant 856559) under the European Community's Horizon 2020 Framework Programme. We thank the support from Dr. Michael Plötze and Markus Rast on measuring pore size distribution and grain density. Grant from CCTEG Coal Mining Research Institute, China (No. TDKC-2022-QN-02 and TDKC-2022-MS-01) and National Natural Science Foundation of China (NSFC) (No. 52274123) is thanked.

Appendix A. Uncertainty analysis in density and porosity

Uncertainties in the density and porosity were subject to the original measurement error (dimension, volume, mass, etc.) on the selected specimen. These original measurements were assumed to be performed independently and randomly. We considered the uncertainty propagation and defined the final uncertainties as the quadratic sum of the original uncertainties⁸⁹, Chapter 3.

We measured the grain density (ρ_{gr}) over two prismoid oven-dried specimens (dimension: 25 mm × 25 mm × 40 mm). The uncertainty in the grain density originated from the measurement of (1) specimen volume using a helium pycnometer and (2) specimen weight. The volume and weight were measured at a standard deviation of 0.012 to 0.024 cm³, and a precision of 0.001 g. The uncertainty ($\frac{\delta \rho_{gr}}{\rho_{gr}}$) in the grain density is given as:

$$\frac{\delta \rho_{gr}}{\rho_{gr}} = \sqrt{\left(\frac{\delta V}{V}\right)^2 + \left(\frac{\delta m}{m}\right)^2}. \quad (4)$$

This resulted an uncertainty of 0.05 to 0.1% (0.0014 to 0.0027 g/cm³) in the grain density.

We estimated the uncertainties in the bulk density (ρ_b) and total porosity (ϕ) over oven-dried cylinders ($L=100$ mm in length, $d=50$ mm in diameter). Specimen dimensions were independently measured at a precision of 0.01 mm. Their volumes (V) are given as $V = \pi d^2 L/4$. The uncertainty ($\frac{\delta V}{V}$) in volumes is defined as:

$$\frac{\delta V}{V} = \sqrt{\left(\frac{2\delta d}{d}\right)^2 + \left(\frac{\delta L}{L}\right)^2}. \quad (5)$$

This resulted an uncertainty ($\frac{\delta V}{V}$) in volumes of around 0.04% (or 0.08 cm³ for cylinder). Bulk density (ρ_b) was calculated using the ratio of weight (m) to volume (V) of the oven-dried cylinder specimen. The weight was measured at a precision of 0.01 g. The uncertainty ($\frac{\delta \rho_b}{\rho_b}$)

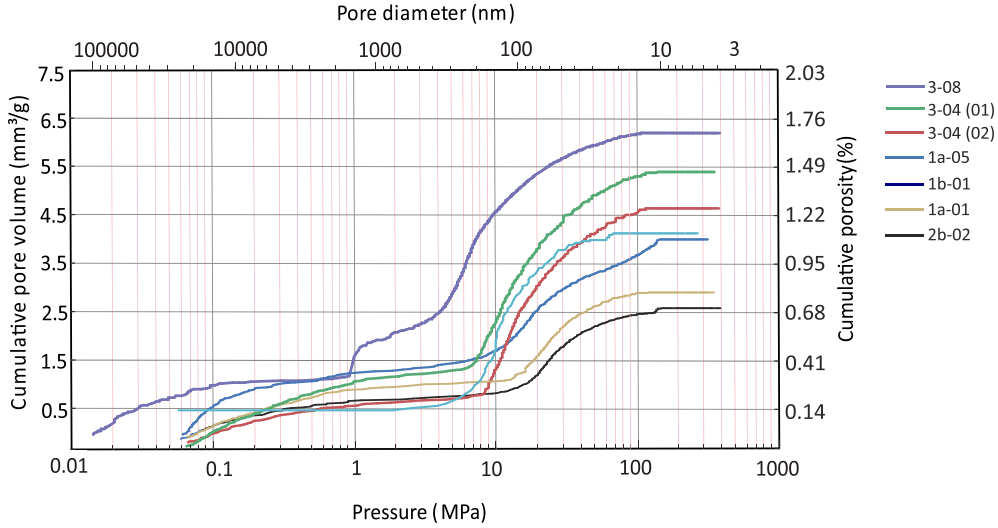


Fig. 12. Cumulative volume of intrusive mercury and mercury-accessible porosity as a function of pressure over seven specimens.
Source: Adapted with permission⁴⁴ (CC BY-NC-ND 4.0).

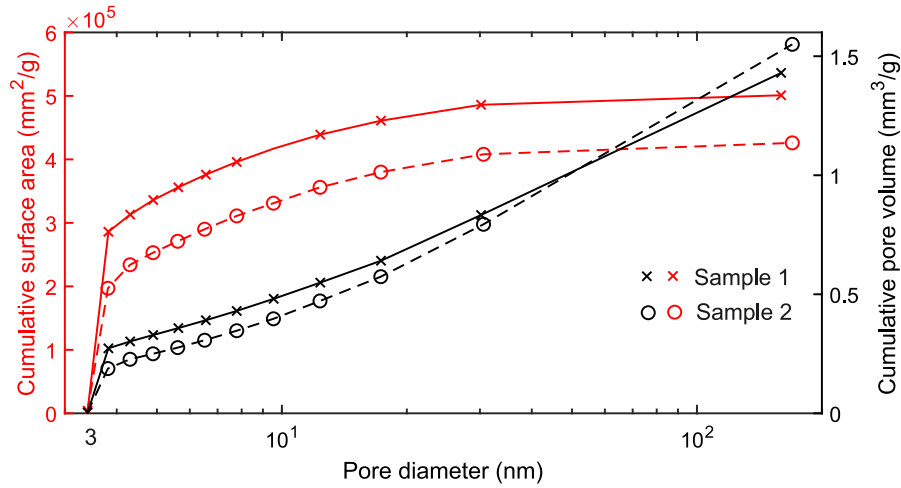


Fig. 13. Cumulative pore surface area and volume as a function of pore diameter during nitrogen adsorption over two specimens.
Source: Adapted with permission.⁴⁸

in the bulk density is given as:

$$\frac{\delta \rho_b}{\rho_b} = \sqrt{\left(\frac{\delta m}{m}\right)^2 + \left(\frac{\delta V}{V}\right)^2} \quad (6)$$

and calculated as around 0.04% (or 0.001 g/cm³).

The total porosity (ϕ_t) was derived from the difference between the grain and bulk density as $\phi_t = 1 - \rho_b/\rho_s$. Its uncertainty is given as:

$$\frac{\delta \phi_t}{\phi_t} = \frac{1}{\rho_s - \rho_b} \sqrt{\left(\frac{\rho_b}{\rho_s} \delta \rho_s\right)^2 + (\delta \rho_b)^2} \quad (7)$$

and calculated as 0.2% over the granite cylinders. This uncertainty is relatively large to the measured ϕ_t (1.9%).

The water-accessible porosity (ϕ_w) was calculated from the ratio of the mass difference between oven-dried and vacuum-saturated cylinder specimen and the volume. Its uncertainty is given as:

$$\frac{\delta \phi_w}{\phi_w} = \sqrt{\left(\frac{\delta m_o}{m_w - m_o}\right)^2 + \left(\frac{\delta m_w}{m_w - m_o}\right)^2 + \left(\frac{\delta V}{V}\right)^2} \quad (8)$$

and calculated as 0.007% in the total volume of the cylinder specimen. This also suggested that the measurement of ϕ_w is more precise than ϕ_t .

Appendix B. Porosimetry through mercury intrusion and nitrogen adsorption

Seven prismoid specimens (20 mm × 6.5 mm × 6.5 mm) were prepared for the mercury porosimetry. Mercury was intruded into the pore spaces up to 400 MPa and its cumulative volume (V_{Hg}) was shown as a function of pressure on the left side in Fig. 12 (adapted with permission⁴⁴). The cumulative volumes were measured between 2.59 to 6.21 mm³/g at a precision of 0.01 mm³/g over seven specimens. The mercury-accessible porosity can be given as $\phi_{Hg} = V_{Hg} \phi_b / 1000$ and was shown on the right side in Fig. 12. ρ_b was the bulk density with an estimated uncertainty of 0.006 g/cm³ following Eq. (6). Mercury-accessible porosity ranged from 0.72% to 1.69% with a mean porosity of around 1.15%. The uncertainty in the mercury-accessible porosity is given as:

$$\frac{\delta \phi_{Hg}}{\phi_{Hg}} = \sqrt{\left(\frac{\delta V_{Hg}}{V_{Hg}}\right)^2 + \left(\frac{\delta \rho_b}{\rho_b}\right)^2} \quad (9)$$

and $\delta \phi_{Hg}$ was calculated between 0.003% to 0.005% in the total volume of the prismoid specimen for individual measurement. Washburn's equation was adopted to calculate the pore size from the pressure by assuming the cylindrical pore spaces⁵³ (see the upper axis

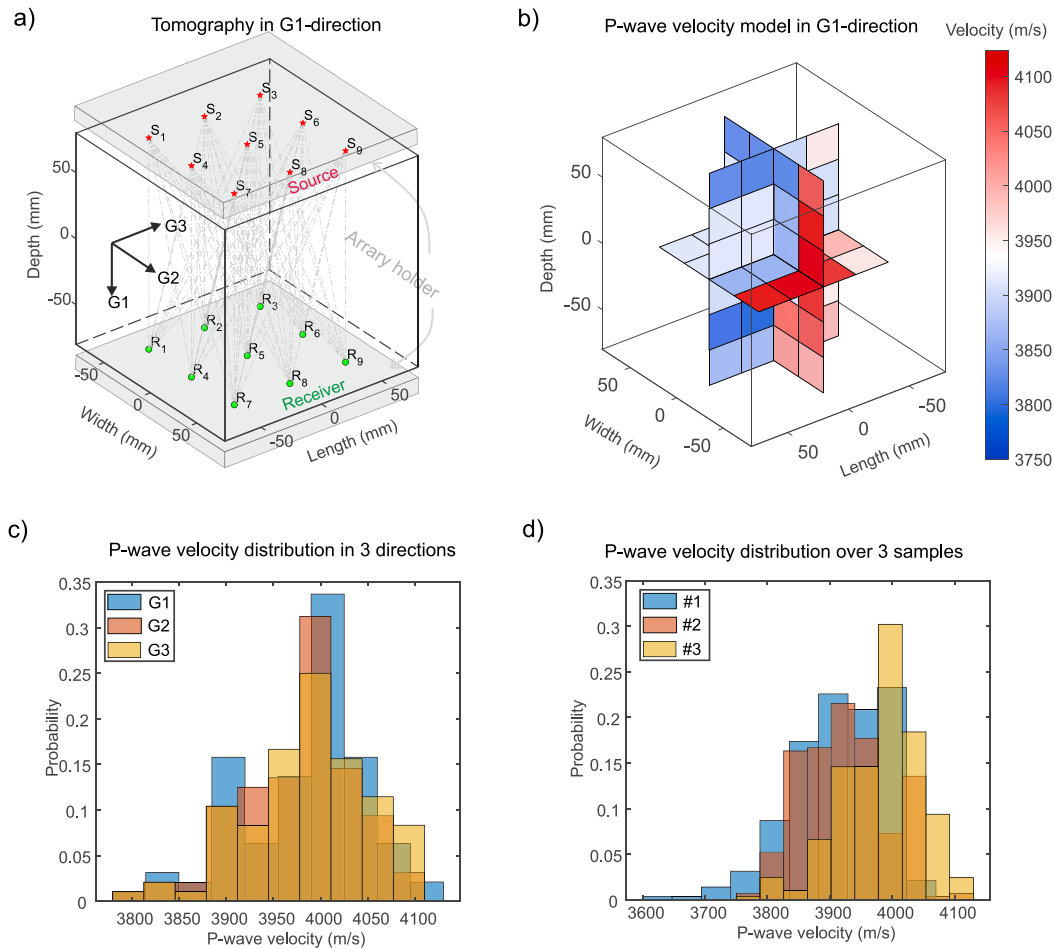


Fig. 14. (a) General schematic of the setup to measure P-wave velocity tomography using travel-time tomography. (b) Reconstructed P-wave velocity slices along the $G1$ direction. (c) P-wave velocity histograms along the $G1$, $G2$ and $G3$ directions for 1 specimen. (d) P-wave velocity histograms for the three specimens.

of Fig. 12). Around 70% of mercury-accessible pore diameters falling below 200 nm.⁴⁴ Although Washburn's equation holds for the penetration of mercury through pore throats greater than around 3 nm,⁵³ intruded mercury volume maintained when the throat diameter was lower around 10 nm. Poorly connected pores and pores with a throat diameter less than 10 nm were not open to mercury even at intrusive pressures up to 400 MPa. These pore volumes were not counted into the mercury-accessible porosity, and could possibly contribute to the difference between the total ($1.9\% \pm 0.2\%$) and mercury-accessible porosity.

To quantify the pore size distribution below 10 nm, researchers⁴⁸ conducted the porosimetry of nitrogen adsorption over two specimens ($40 \text{ mm} \times 10.5 \text{ mm} \times 10.5 \text{ mm}$). In Fig. 13, they showed cumulative surface area (red) and pore volume (black) as a function of pore diameter during the nitrogen adsorption over two specimens (symbol cross and circle). They found that around 80% of the surface area of this granite exhibited a pore diameter below 10 nm.

Appendix C. P-wave velocity measurement

A suite of characterization tests was performed to measure P-wave velocity structure under ambient conditions. We performed 3D ultrasonic tomography⁵⁴ on three cuboidal specimens of granite with a side length of 160 mm under ambient conditions. Three dimensions were along the principle splitting directions and denoted as $G1$, $G2$ and $G3$. The travel time information of the first P-wave arrivals from the transmitters to receivers was used. In Fig. 14(a), we showed a schematic representation of the ultrasonic tomography setup along the

$G1$ direction. An array of nine in-house piezoelectric (PZT) transmitter (model: PCT-MCX)⁷² and nine passive PZT receivers (model: KRNB-PC)⁷³ were mounted in two separate aluminum array holders (gray blocks, Fig. 14(a)). PZT transmitters and receivers were in contact with the top and bottom surfaces of the granite cube, respectively. A 300 V impulse source, with a duration of 1 μs , was applied to these PZT transmitters using a pulsing unit (HVP, Elsys Instruments AE-HV-MUX). Each transmitter emitted an impulse source in a sequential manner that was repeated 10 times for each transmitter. Waveforms on the receivers were recorded in the data acquisition system (DAQ) at a sampling rate of 20 MHz and 16 bit resolution (Elsys Instruments TraNET/Lab-AX). This DAQ system was used in the water imbibition experiments.

The specimens were modeled as $6 \times 6 \times 6$ cubic elements each having dimensions of $26.7 \text{ mm} \times 26.7 \text{ mm} \times 26.7 \text{ mm}$. We assumed that the waves propagating from transmitter to receiver were approximated by straight rays. The P-wave travel time and distance of each transmitter-receiver pair were stored in two 9×9 arrays, respectively. P-wave velocity structure was derived at the center of each cubic cell using the Moore-Penrose pseudoinverse. More detail and the mathematical description of the inversion problem is referred.⁵⁴ To determine the onset of the P-wave arrival at each receiver, we used the Aikake information criterion (AIC)⁵⁵ that has been effective in laboratory ultrasonic studies.⁷⁷

In Fig. 14(a), there were 81 straight ray paths (dashed gray lines) that sample most of the cells between transmitters and receivers. In Fig. 14(b), we showed the P-wave velocity structure along the $G1$ direction, and no obvious heterogeneity was observed (standard deviation: 68.5 m/s, 1.72% of the mean value) among cells. Note that the P-wave

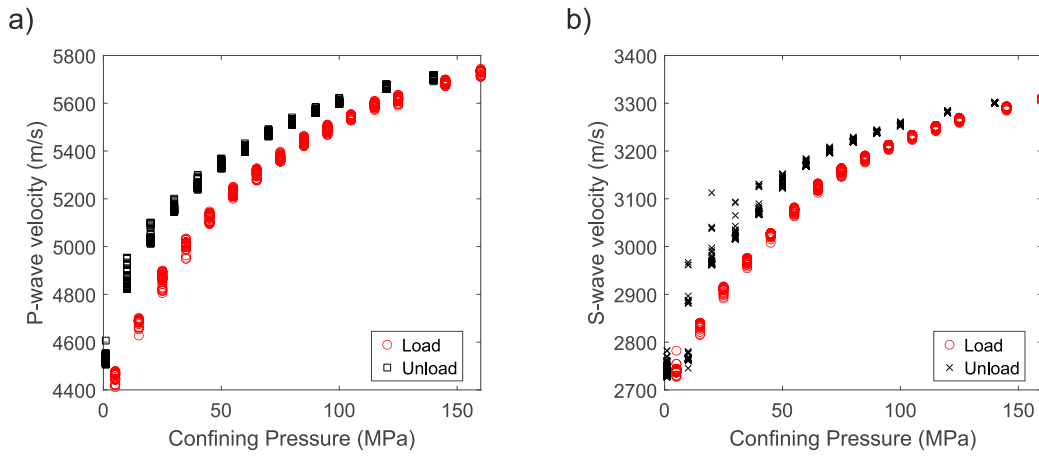


Fig. 15. P- (left) and S-wave (right) velocity changes in dry Herrnholz granite in response to a series of confining pressures during the loading (red) and unloading (black) stage. (For interpretation of the references to color in this figure legend, the reader is referred to the web version of this article.)

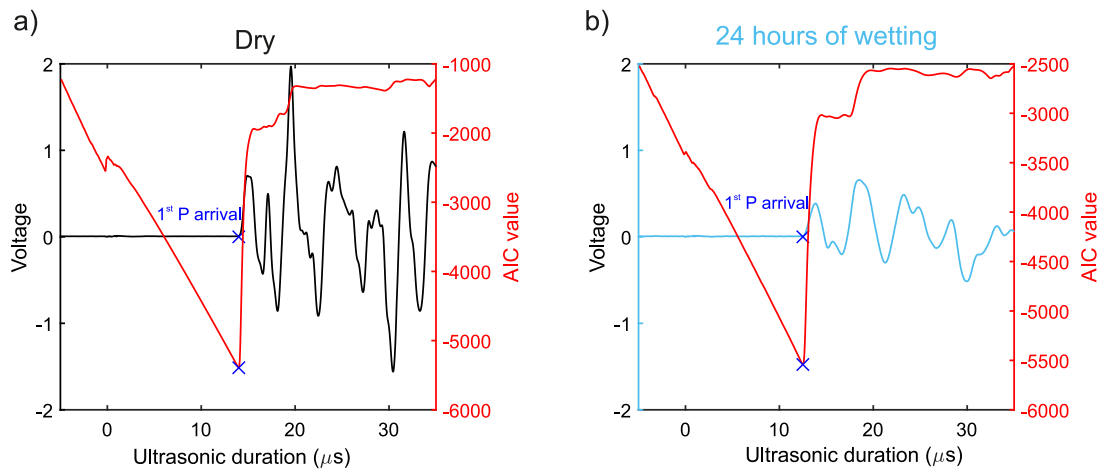


Fig. 16. Raw transmitted waveforms and their AIC values under (a) dry and (b) wet conditions. The onset of P-wave first arrival (blue cross) was marked at the position of minimum AIC. (For interpretation of the references to color in this figure legend, the reader is referred to the web version of this article.)

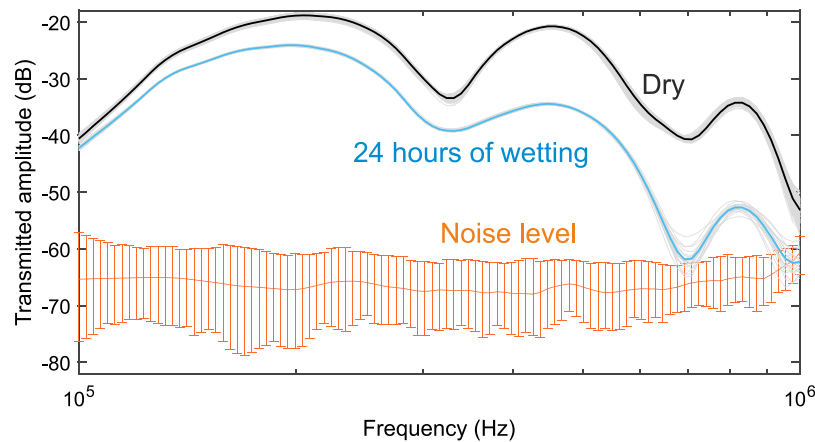


Fig. 17. Transmitted amplitude (dB) of windowed waveforms in the frequency domain shown in Fig. 4(d) measured (a) under dry conditions and (b) after 24 h of wetting. Noise level is given as the reference. Transmitted amplitude above 1 MHz after 24 h of wetting is hard to be differentiable from the noise level.

velocities were omitted in the cells near the outer surfaces (G2 and G3) because of the lack of effective coverage of straight rays.

To check the seismic anisotropy, this procedure was repeated in the G2 and G3 directions. P-wave velocity in each orthogonal direction was characterized by 3981 ± 69 , 3977 ± 60 , and 3988 ± 64 m/s, respectively. The uncertainty was estimated as 1.72%, 1.53%, and

1.60%, respectively. Single-peaked normal (or Gaussian) distributions with very close peak values (around 3997, 3995, and 3995 m/s) were shown in the probability density functions of Fig. 14(c). To avoid specimen variability, we repeated the tests on the other 2 specimens, and the overlapping probability histograms of P-wave velocity distribution were presented in Fig. 14(d). P-wave velocities were 3914 ± 74 , $3925 \pm$

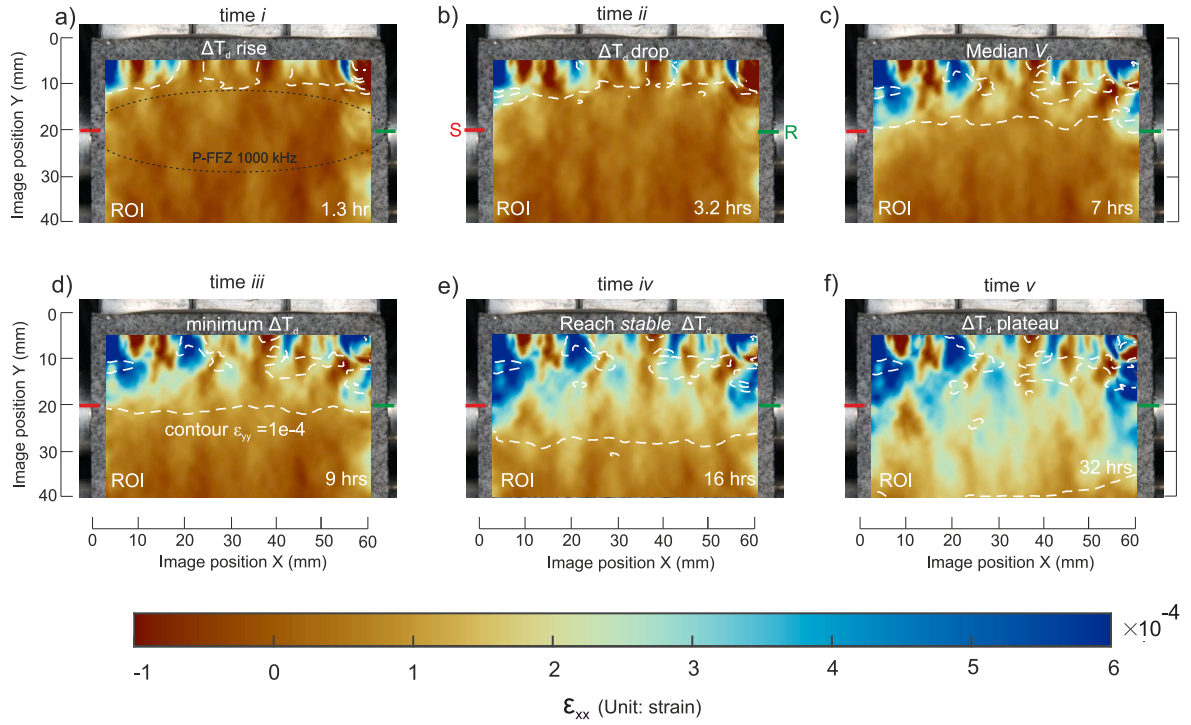


Fig. 18. Horizontal strain (ϵ_{xx}) evolution on the front surface (ROI: 58 mm in width and 40 mm in height) with water being applied to the granite specimen. 0 h denotes the time that water is applied to the top surface of the specimen. Stage i to v are time moments previously defined in the acoustic signature analysis.

71, and 3982 ± 64 m/s, respectively. The uncertainty was estimated as 1.9%, 1.8% and 1.6%, respectively. We can therefore conclude that there was very weak anisotropy, heterogeneity, and specimen variability in the elastic wave velocities of Herrnholz granite.

Appendix D. Hydrostatic compression test

To further characterize the material, stress dependence tests of the elastic properties of Herrnholz granite were conducted. This was necessary to provide input data for the validation of the elastic modulus dispersion model in saturated nanopore-dominated rocks employed later.

Hydrostatic compression tests were repeated on two Herrnholz granite and one aluminum cylinders (100 mm in length and 50 mm in diameter) that underwent a stepwise increase in confining pressure from 0 to 160 MPa. The Herrnholz granite specimens were tested under both oven-dried and fully saturated conditions. The aluminum specimen was the reference test, using the same loading procedures. Specimens were tightly wrapped in a rubber jacket and placed into a conventional triaxial machine, LabQuake, located in the Rock Physics and Mechanics Laboratory at ETH Zurich.⁹⁰ The system can achieve confining pressures up to 170 MPa and exhibits a minimum frame stiffness of 2500 kN/mm. P- and S-wave transmitter-receiver pairs, installed in the two loading platens, were assembled with specimens at two ends to generate P or S waves at a resonant frequency of approximately 1 MHz through the specimen in the axial direction.

During the test, the confining pressure was increased at a loading rate of 5 MPa/min and was maintained at a series of levels (5, 15, 25, ..., 160 MPa). The elastic stiffening of the rock specimen in response to the increased pressure was probed by P and S waves. A “square” pulse was emitted every 30 s with a duration of 1 μ s and a maximum voltage of 12 V. During each loading step, the wave velocity showed low levels of “drift”. To accommodate for this, we set the duration of the maintained pressure at 30 min.⁶⁹

Appendix E. Uncertainty analysis in wave velocity

Wave velocity (V) was calculated using the ratio of the specimen length (L) to the transmitted time (t). We found the possible original errors could be: (1) measurement precision (L_{pre}) of specimen length, 0.01 mm; (2) parallel tolerance (δL_{para}) between the opposite surfaces, ± 0.025 mm; (3) specimen deformation (L_{deform}) during the test; (4) error in picking arrival times (δt , sampling time). The wave velocity uncertainty can be given using the propagation of error as the quadratic sum of the original uncertainties⁸⁹:

$$\frac{\delta V}{V} = \sqrt{\left(\frac{L_{pre}}{L}\right)^2 + \left(\frac{L_{para}}{L}\right)^2 + \left(\frac{L_{deform}}{L}\right)^2 + \left(\frac{\delta t}{t}\right)^2}. \quad (10)$$

For wave velocity measured along the cylinder specimen during the hydrostatic compression tests, L_{deform} has a maximum value of around 0.3 mm at a confining pressure of 160 MPa. The sampling time was 20 ns. We calculated the uncertainties as around 0.32% (or 18 m/s) for P waves and 0.31% (or 10 m/s) for S waves, respectively.

For wave velocity measured across the prismoid specimen during the free-standing wetting test, maximum $\frac{L_{deform}}{L}$ was around 2.5×10^{-4} near the transmitter-receiver pair, determined from DIC observation in Section 4.2, due to the hygroscopic expansion. The sampling time was 50 ns. The uncertainty in the P-wave velocity was estimated as around 0.25% (or 13 m/s).

Appendix F. Elastic piezosensitivity analysis

Stress dependence of elasticity caused by microcracks in brittle rocks can be described as³⁵:

$$K_{dr}(P_c) = K_{drs}[1 + \theta_s(C_{drs} - C_{gr})P_c - \theta_c\phi_{c0}\exp(-\theta_c P_c C_{drs})], \quad (11a)$$

$$G_{dr}(P_c) = G_{drs}[1 + \theta_{sg}(C_{drs} - C_{gr})P_c - \theta_{cg}\phi_{c0}\exp(-\theta_c P_c C_{drs})], \quad (11b)$$

where K_{dr} , G_{dr} and P_c were measured in the hydrostatic compression tests. The pore space of the rock (ϕ) was assumed to consist of stiff and compliant/crack pores, which formed a fully interconnected pore space.

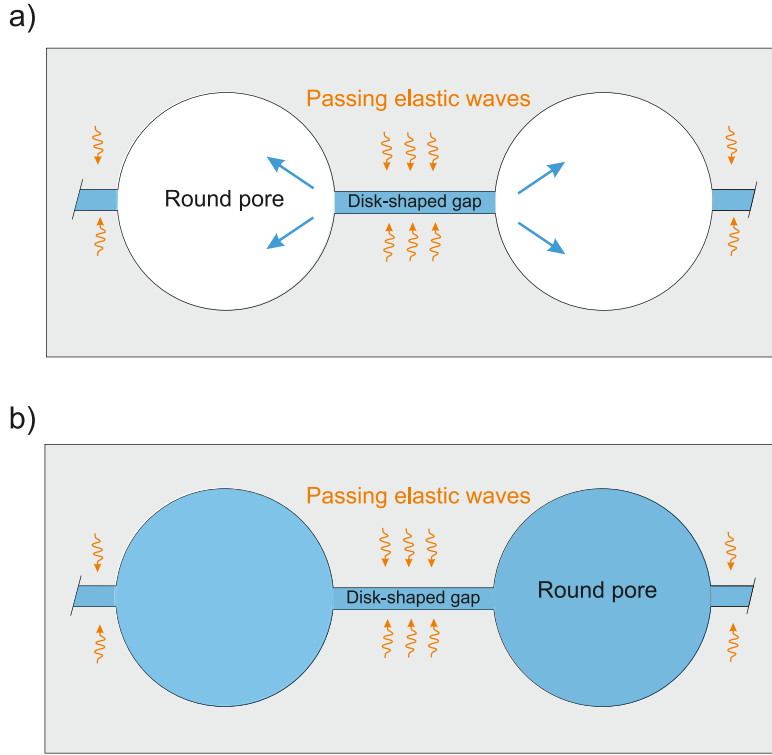


Fig. 19. Schematic diagram of the pore space configuration in microcracked media. A disk-shaped gap (soft pore) represents microcrack between two grains and its edge opens into two round pores (or stiff pores). (a) microcrack is filled with water while the round pores are dry. (b) Both microcrack and round pores are filled with water.

ϕ_{c0} denoted the compliant porosity without confinement: the porosity of the stiff pores (ϕ_s) approximated the water-accessible porosity (ϕ_w). The bulk (K_{gr}) and shear (G_{gr}) moduli of granite without pore space in terms of constituents and pore space from Hill average was 49.4 and 31.1 GPa, respectively. We provided the mineral moduli and effective elastic moduli of Herrnholz granite in Table 2. K_{drs} and G_{drs} were the bulk and shear moduli of a hypothetical rock in the case of a closed compliant porosity ($\phi_c \approx 0$). C_{gr} and C_{drs} are the compressibilities, the reciprocal of K_{gr} and K_{drs} , respectively.

From left to right in Eqs. (11a) and (11b), 1, linear term and exponential term represented the individual contribution from mineral grains, stiff pores and compliant cracks to moduli, respectively. θ_c and θ_{cg} were the elastic sensitivity of confining pressure on the exponential term of bulk and shear moduli $O(10^2)$, while θ_s and θ_{sg} with the order of $O(1)$ reflected the sensitivity of linear terms:

$$\theta_s = -\frac{1}{K_{drs}} \frac{\partial K_{dr}}{\partial \phi_s}, \quad \theta_c = -\frac{1}{K_{drs}} \frac{\partial K_{dr}}{\partial \phi_c}, \quad (12a)$$

$$\theta_{s\mu} = -\frac{1}{\mu_{drs}} \frac{\partial \mu_{dr}}{\partial \phi_s}, \quad \theta_{c\mu} = -\frac{1}{\mu_{drs}} \frac{\partial \mu_{dr}}{\partial \phi_c} \quad (12b)$$

Inputting the measured K_{dry} , G_{dry} and P_c and given the initial guesses for the unknown parameters K_{drs} , G_{drs} , θ_s , θ_{sg} , θ_c , θ_{cg} and ϕ_{c0} , the residuals of Eqs. (11a) and (11b) were obtained, summed and minimized to find optimal parameters: $K_{drs} = 49.7$ GPa, $G_{drs} = 29.7$ GPa, $\theta_s = 6.2 \times 10^{-4}$, $\theta_{sg} = 4.8 \times 10^{-4}$, $\theta_c = 701$, $\theta_{cg} = 505$ and $\phi_{c0} = 7.2 \times 10^{-4}$.

The observation of $\theta_s \phi_s \ll \theta_c \phi_c$ (ratio: 1.9×10^{-5}) suggested that the elastic variations strongly depended on changes in the compliant porosity and only depend weakly on changes in the stiff porosity. By assuming that the cracks were penny-shaped within the framework of effective medium theories, the representative aspect ratio α was estimated at approximately 1.1×10^{-3} (Equation 11³⁵; more detail⁵⁸):

$$\alpha \approx \frac{K_{gr}(3K_{gr} + 4\mu_{gr})}{\pi\theta_c\mu_{gr}(3K_{gr} + \mu_{gr})}. \quad (13)$$

Appendix G. P-wave velocity increase from squirt flow model

In this section, we detailed the calculation procedures of P-wave velocity increase at all frequencies in saturated microcracked porous media using a squirt flow model.²⁰ We showed a schematic diagram of the pore space configuration in microcracked media in Fig. 19. The pore space of the rock is assumed to consist of stiff (or round) and compliant pores, which form a fully interconnected pore space. A disk-shaped gap (soft pore) represents microcrack between two grains and its tip opens into two adjacent round pores (or stiff pores). The gap is assumed to have asperities so that it has a finite stiffness even when the gap is dry. When elastic waves propagate in such a configuration, infilled water does not have sufficient time to escape from the gap within the half-period of the wave. This gives a frequency-dependent bulk modulus $K_f^*(\omega)$ of water:

$$K_f^*(\omega) = \left[1 - \frac{2J_1(ka)}{kaJ_0(ka)} \right] K_f, \quad (14)$$

where ω is angular frequency, a is disk radius, J_0 and J_1 are Bessel equation of zero order and first order, K_f is bulk modulus of water. k is wavenumber and is given as $k^2 = -\frac{12i\omega\eta}{h_0^2 K_f}$. h_0 is the disk thickness and disappears together with disk radius a in Eq. (14) using the aspect ratio $\alpha = \frac{h_0}{2a}$ that is available (1.1×10^{-3}) from elastic piezosensitivity analysis. η is the dynamic viscosity of water (9.4×10^{-4} Pa·s under 23 °C and 1 standard atmosphere).

In Fig. 19(a), microcrack was filled with water while the round pores were dry. By applying Gassmann equations, researchers⁹¹ derived the partially relaxed bulk modulus K_{mf} and shear modulus G_{mf} of this modified frame under a confining pressure P as:

$$\frac{1}{K_{mf}(P, \omega)} = \frac{1}{K_{drs}} + \frac{\phi_c(P) \left(\frac{1}{K_f^*(P, \omega)} - \frac{1}{K_{gr}} \right)}{1 + \phi_c(P) \left(\frac{1}{K_f^*(P, \omega)} - \frac{1}{K_{gr}} \right) / \left(\frac{1}{K_{dry}(P)} - \frac{1}{K_{drs}} \right)}, \quad (15a)$$

$$\frac{1}{G_{mf}(P, \omega)} = \frac{1}{G_{dry}(P)} - \frac{4}{15} \left[\frac{1}{K_{dry}(P)} - \frac{1}{K_{mf}(P, \omega)} \right], \quad (15b)$$

Table 2

Mineral moduli and effective elastic moduli of Herrnholz granite.

	Quartz	Feldspar (plagioclase)	Mica (Biotite)	Voigt bound		Reuss bound	Hill average
Fraction (%)	50	38	11				
Bulk modulus (GPa)	37	75.6	41.1	51.7		47.1	49.4
Shear modulus (GPa)	44	25.6	13.4	33.2		29.1	31.1

Moduli of common minerals.¹⁰

Table 3

Summary of ultrasonic attribute changes through the gradual wetting process.

Acoustic changes	Symbol	Unit	Freq	Stages					Total
				O	i	ii	iii	iv	
Transmitted amplitude	ΔT_d	dB	LF	± 1	± 1	$\uparrow 2.6$	$\downarrow 9$	$\uparrow 0.6$	± 0.1
			MF			$\uparrow 3$	$\downarrow 19.5$	$\uparrow 5.5$	
			HF			$\uparrow 4$	$\downarrow 27$	$\uparrow 8$	
P-wave velocity	ΔV_p	m/s		± 10	$\downarrow 30$		$\uparrow 550$		± 19
Inverse quality factor	$4(1/Q_p)$	1×10^{-3}		± 1	$\uparrow 13$			$\uparrow 37$	± 5

Symbol \pm represents the attribute fluctuation due to the background noise levels in the measurements.

where K_{drs} and K_{gr} were the bulk modulus of hypothetical granite in the case of a closed compliant porosity ($\phi_c \approx 0$) and without pore space, respectively. $K_{dry}(P)$ and $G_{dry}(P)$ were the bulk and shear modulus of dry rocks at different confining pressure, respectively. $K_{dry}(P)$ and $G_{dry}(P)$ were measured from hydrostatic compression tests (Fig. 3(c) and (d)). $\phi_c(P)$ was the compliant porosity at different confining pressure and was available from elastic piezosensitivity analysis (blue dashed line in Fig. 3(c)).

In Fig. 19(b), both microcrack and round pores were filled with water and we applied the Gassmann equation¹¹ again to calculate bulk modulus K_{sat} and shear modulus G_{sat} of this fully saturated granite under a confining pressure P :

$$\frac{1}{K_{sat}(P, \omega)} = \frac{1}{K_{gr}} + \frac{\phi_s \left(\frac{1}{K_f} - \frac{1}{K_{gr}} \right)}{1 + \phi_s \left(\frac{1}{K_f} - \frac{1}{K_{gr}} \right) / \left(\frac{1}{K_{mf}(P, \omega)} - \frac{1}{K_{gr}} \right)}, \quad (16a)$$

$$G_{sat}(P, \omega) = G_{mf}(P, \omega), \quad (16b)$$

where ϕ_s was the porosity of the stiff pores and approximates the water-accessible porosity (ϕ_w). We calculated bulk modulus $K_{sat}(P)$ and shear modulus $G_{sat}(P)$ from the squirt flow model at interested frequency bandwidth – 1 MHz in our study. Theoretical prediction of P-wave velocity $V_p(P)$ under different confining pressure in saturated microcracked media is given as:

$$V_p(P) = \sqrt{\frac{K_{sat}(P) + \frac{4}{3}G_{sat}(P)}{\rho_{sat}}}, \quad (17)$$

where ρ_{sat} was the density (2.63 g/cm^3) of saturated rock and was assumed not to change with confining pressure (see Table 3).

References

- Gor GY, Neimark AV. Adsorption-induced deformation of mesoporous solids. *Langmuir*. 2010;26(16):13021–13027. <http://dx.doi.org/10.1021/la1019247>.
- Gor GY, Bernstein N. Revisiting Bangham's law of adsorption-induced deformation: Changes of surface energy and surface stress. *Phys Chem Chem Phys*. 2016;18(14):9788–9798. <http://dx.doi.org/10.1039/c6cp00051g>.
- Loew S, Gschwind S, Gischig V, Keller-Signer A, Valenti G. Monitoring and early warning of the 2012 Preonzo catastrophic rock slope failure. *Landslides*. 2017;14(1):141–154. <http://dx.doi.org/10.1007/s10346-016-0701-y>.
- Burjáněk J, Gischig V, Moore JR, Fäh D. Ambient vibration characterization and monitoring of a rock slope close to collapse. *Geophys J Int*. 2017;212(1):297–310. <http://dx.doi.org/10.1093/gji/ggx424>.
- Le Breton M, Bontemps N, Guillemot A, Baillet L, Larose E. Landslide monitoring using seismic ambient noise correlation: Challenges and applications. *Earth-Sci Rev*. 2021;216:103518. <http://dx.doi.org/10.1016/J.EARSCIREV.2021.103518>.

- Diederichs MS. The 2003 Canadian geotechnical colloquium: Mechanistic interpretation and practical application of damage and spalling prediction criteria for deep tunnelling. *Can Geotech J*. 2007;44(9):1082–1116. <http://dx.doi.org/10.1139/T07-033>.
- McBain JW, Ferguson J. On the nature of the influence of humidity changes upon the composition of building materials. *J Phys Chem*. 1927;31(4):564–590.
- Landrø M. Discrimination between pressure and fluid saturation changes from time-lapse seismic data. *Geophysics*. 2001;66(3):836–844. <http://dx.doi.org/10.1190/1.1444973>.
- Saito T. Variation of Physical Properties of Igneous Rocks In Weathering. In: *Proceedings of the International Symposium on Weak Rock*. Tokyo: 1981:191–196.
- Mavko G, Mukerji T, Dvorkin J. *The Rock Physics Handbook*. Cambridge, United Kingdom: Cambridge University Press; 1998. <http://dx.doi.org/10.1017/9781108333016>.
- Gassmann F. Elastic waves through a packing of spheres. *Geophysics*. 1951;16(4):673–685. <http://dx.doi.org/10.1190/1.1437718>.
- Nur A, Simmons G. The effect of saturation on velocity in low porosity rocks. *Earth Planet Sci Lett*. 1969;7(2):183–193. [http://dx.doi.org/10.1016/0012-821X\(69\)90035-1](http://dx.doi.org/10.1016/0012-821X(69)90035-1).
- Winkler K, Nur A. Pore fluids and seismic attenuation in rocks. *Geophys Res Lett*. 1979;6(1):1–4. <http://dx.doi.org/10.1029/GL006i001p00001>.
- Toksöz MN, Johnston DH, Timur A. Attenuation of seismic waves in dry and saturated rocks: I. Laboratory measurements. *Geophysics*. 1979;44(4):681–690. <http://dx.doi.org/10.1190/1.1440969>.
- Johnston DH, Toksöz MN, Timur A. Attenuation of seismic waves in dry and saturated rocks: II. Mechanisms. *Geophysics*. 1979;44(4):691–711. <http://dx.doi.org/10.1190/1.1440970>.
- Mavko G, Nur A. Wave attenuation in partially saturated rocks. *Geophysics*. 1979;44(2):161–178. <http://dx.doi.org/10.1190/1.1440958>.
- Murphy III WF. *Effects of Microstructure and Pore Fluids on the Acoustic Properties of Granular Sedimentary Materials* (Ph.D. thesis). Stanford University; 1982.
- Knight R, Nolen-Hoeksema R. A laboratory study of the dependence of elastic wave velocities on pore scale fluid distribution. *Geophys Res Lett*. 1990;17(10):1529–1532. <http://dx.doi.org/10.1029/GL017i010p01529>.
- Walsh JB. Seismic attenuation in partially saturated rock. *J Geophys Res: Solid Earth*. 1995;100(B8):15407–15424. <http://dx.doi.org/10.1029/94JB03264>.
- Gurevich B, Makarynska D, de Paula OB, Pervukhina M. A simple model for squirt-flow dispersion and attenuation in fluid-saturated granular rocks. *Geophysics*. 2010;75(6):N109–N120. <http://dx.doi.org/10.1190/1.3509782>.
- Thommes M, Kaneko K, Neimark AV, et al. Physiosorption of gases, with special reference to the evaluation of surface area and pore size distribution (IUPAC Technical Report). *Pure Appl Chem*. 2015;87(9–10):1051–1069. <http://dx.doi.org/10.1515/pac-2014-1117>.
- King MS. Wave velocities in rocks as a function of changes in overburden pressure and pore fluid saturants. *Geophysics*. 1966;31(1):50–73. <http://dx.doi.org/10.1190/1.1439763>.
- Han D-H. *Effects of Porosity and Clay Content on Acoustic Properties of Sandstones and Unconsolidated Sediments* (Ph.D. thesis). Stanford University; 1987.
- Coyner KB. *Effects of Stress, Pore Pressure, and Pore Fluids on Bulk Strain, Velocity, and Permeability in Rocks* (Ph.D. thesis). Massachusetts Institute of Technology; 1984.
- Mavko G, Jizba D. Estimating grain-scale fluid effects on velocity dispersion in rocks. *Geophysics*. 1991;56(12):1940–1949. <http://dx.doi.org/10.1190/1.1443005>.

26. Wang L, Rybacki E, Bonnelye A, Bohnhoff M, Dresen G. Experimental investigation on static and dynamic bulk moduli of dry and fluid-saturated porous sandstones. *Rock Mech Rock Eng.* 2021;54(1):129–148. <http://dx.doi.org/10.1007/s00603-020-02248-3>.
27. Agersborg R, Johansen TA, Jakobsen M, Sothcott J, Best A. Effects of fluids and dual-pore systems on pressure-dependent velocities and attenuations in carbonates. *Geophysics.* 2008;73(5):N35–N47. <http://dx.doi.org/10.1190/1.2969774>.
28. Biot MA. Theory of propagation of elastic waves in a fluid saturated porous solid. I. Low frequency range and II. Higher-frequency range. *J Acoust Soc Am.* 1956;28(2):168–191. <http://dx.doi.org/10.1121/1.1908241>.
29. Müller TM, Gurevich B, Lebedev M. Seismic wave attenuation and dispersion resulting from wave-induced flow in porous rocks - A review. *Geophysics.* 2010;75(5). <http://dx.doi.org/10.1190/1.3463417>.
30. Gor GY, Gurevich B. Gassmann theory applies to nanoporous media. *Geophys Res Lett.* 2018;45(1):146–155. <http://dx.doi.org/10.1002/2017GL075321>.
31. Page JH, Liu J, Abeles B, Herbolzheimer E, Deckman HW, Weitz DA. Adsorption and desorption of a wetting fluid in Vycor studied by acoustic and optical techniques. *Phys Rev E.* 1995;52(3):2763–2777. <http://dx.doi.org/10.1103/PhysRevE.52.2763>.
32. Schappert K, Pelster R. Elastic properties of liquid and solid argon in nanopores. *J Phys: Condens Matter.* 2013;25(41):415302. <http://dx.doi.org/10.1088/0953-8984/25/41/415302>.
33. Berryman JG. Origin of Gassmann's equations. *Geophysics.* 1999;64(5):1627–1629. <http://dx.doi.org/10.1190/1.1444667>.
34. Levitz P, Ehret G, Sinha SK, Drake JM. Porous vycor glass: The microstructure as probed by electron microscopy, direct energy transfer, small-angle scattering, and molecular adsorption. *J Chem Phys.* 1991;95(8):6151–6161. <http://dx.doi.org/10.1063/1.461583>.
35. Shapiro SA. Elastic piezosensitivity of porous and fractured rocks. *Geophysics.* 2003;68(2):482–486. <http://dx.doi.org/10.1190/1.1567215>.
36. O'Connell RJ, Budiansky B. Viscoelastic properties of fluid-saturated cracked solids. *J Geophys Res.* 1977;82(36):5719–5735. <http://dx.doi.org/10.1029/JB082i036p05719>.
37. Dobrzanski CD, Gurevich B, Gor GY. Elastic properties of confined fluids from molecular modeling to ultrasonic experiments on porous solids. *Appl Phys Rev.* 2021;8(2):21317. <http://dx.doi.org/10.1063/5.0024114>.
38. Winkler K, Nur A. Seismic attenuation: Effects of pore fluids and frictional-sliding. *Geophysics.* 1982;47(1):1–15. <http://dx.doi.org/10.1190/1.1441276>.
39. Wulff A, Mjaaland S. Seismic monitoring of fluid fronts: An experimental study. *Geophysics.* 2002;67(1):221–229. <http://dx.doi.org/10.1190/1.1451622>.
40. Lopes S, Lebedev M, Müller TM, Clennell MB, Gurevich B. Forced imbibition into a limestone: Measuring P-wave velocity and water saturation dependence on injection rate. *Geophys Prospect.* 2014;62(5):1126–1142. <http://dx.doi.org/10.1111/1365-2478.12111>.
41. David C, Sarout J, Dautriat J, et al. Ultrasonic monitoring of spontaneous imbibition experiments: Precursory moisture diffusion effects ahead of water front. *J Geophys Res: Solid Earth.* 2017;122(7):4948–4962. <http://dx.doi.org/10.1002/2017JB014193>.
42. Pimienta L, David C, Sarout J, Perrot X, Dautriat J, Barnes C. Evolution in seismic properties during low and intermediate water saturation: Competing mechanisms during water imbibition? *Geophys Res Lett.* 2019;46(9):4581–4590. <http://dx.doi.org/10.1029/2019GL082419>.
43. Thery R, Guillemot A, Abraham O, Larose E. Tracking fluids in multiple scattering and highly porous materials: Toward applications in non-destructive testing and seismic monitoring. *Ultrasonics.* 2020;102:106019. <http://dx.doi.org/10.1016/j.ultras.2019.106019>.
44. Li Y, Leith K, Perras MA, Loew S. Digital image correlation-based analysis of hygroscopic expansion in Herrnholt granite. *Int J Rock Mech Min Sci.* 2021;146:104859. <http://dx.doi.org/10.1016/j.ijrmms.2021.104859>.
45. Yurikov A, Lebedev M, Gor GY, Gurevich B. Sorption-induced deformation and elastic weakening of Bentheim sandstone. *J Geophys Res: Solid Earth.* 2018;123(10):8589–8601.
46. Tiennot M, Fortin J. Moisture-induced elastic weakening and wave propagation in a clay-bearing sandstone. *Géotechn Lett.* 2020;10(3):424–428.
47. Saenger EH, Lebedev M, Uribe D, et al. Analysis of high-resolution X-ray computed tomography images of Bentheim sandstone under elevated confining pressures. *Geophys Prospect.* 2016;64(4):848–859. <http://dx.doi.org/10.1111/1365-2478.12400>.
48. Li Y, Leith K, Perras MA, Loew S. Effect of ambient humidity on the elasticity and deformation of unweathered granite. *J Geophys Res: Solid Earth.* 2022;127(11):e2022JB024004. <http://dx.doi.org/10.1029/2022JB024004>.
49. Voigt W. *Lehrbuch Der Kristallphysik (Mit Ausschluss Der Kristalloptik)*, vol. 34. BG Teubner; 1910.
50. Reuss A. Computation of the yield point of mixed crystals due to hiring for single crystals. *Math Phys.* 1929;9:49–58.
51. Hill R. The elastic behaviour of a crystalline aggregate. *Proc Phys Soc Sec A.* 1952;65(5):349–354. <http://dx.doi.org/10.1088/0370-1298/65/5/307>.
52. Selvadurai, Letendre A, Hekimi B. Axial flow hydraulic pulse testing of an argillaceous limestone. *Environ Earth Sci.* 2011;64(8):2047–2058. <http://dx.doi.org/10.1007/s12665-011-1027-7>.
53. Washburn EW. The dynamics of capillary flow. *Phys Rev.* 1921;17(3):273–283. <http://dx.doi.org/10.1103/PhysRev.17.273>.
54. Martiartu NK, Böhm C. Ttomo: Straight ray tomography. 2017 URL <https://cos.ethz.ch/software/research/ttomo.html>.
55. Akaike H. A new look at the statistical model identification. *IEEE Trans Automat Control.* 1974;19(6):716–723. <http://dx.doi.org/10.1109/TAC.1974.1100705>.
56. Christeson GL, Gulick SP, Morgan JV, et al. Extraordinary rocks from the peak ring of the Chicxulub impact crater: P-wave velocity, density, and porosity measurements from IODP/ICDP Expedition 364. *Earth Planet Sci Lett.* 2018;495:1–11. <http://dx.doi.org/10.1016/J.EPSL.2018.05.013>.
57. Pyrak-Nolte LJ, Myer LR, Cook NG. Transmission of seismic waves across single natural fractures. *J Geophys Res.* 1990;95(B6):8617–8638. <http://dx.doi.org/10.1029/JB095i06p08617>.
58. O'Connell RJ, Budiansky B. Seismic velocities in dry and saturated cracked solids. *J Geophys Res (1896-1977).* 1974;79(35):5412–5426. <http://dx.doi.org/10.1029/JB079i035p05412>.
59. Adams LH, Williamson ED. On the compressibility of minerals and rocks at high pressures. *J Franklin Inst B.* 1923;195(4):475–529. [http://dx.doi.org/10.1016/S0016-0032\(23\)90314-5](http://dx.doi.org/10.1016/S0016-0032(23)90314-5).
60. Brace WF. Some new measurements of linear compressibility of rocks. *J Geophys Res (1896-1977).* 1965;70(2):391–398. <http://dx.doi.org/10.1029/JZ070i002p00391>.
61. Wepfer WW, Christensen NI. A seismic velocity-confining pressure relation, with applications. *Int J Rock Mech Min Sci Geomech Abstracts.* 1991;28(5):451–456. [http://dx.doi.org/10.1016/0148-9062\(91\)90083-X](http://dx.doi.org/10.1016/0148-9062(91)90083-X).
62. Walsh JB. The effect of cracks on the compressibility of rock. *J Geophys Res (1896-1977).* 1965;70(2):381–389. <http://dx.doi.org/10.1029/JZ070i002p00381>.
63. Cheng CH, Toksöz MN. Inversion of seismic velocities for the pore aspect ratio spectrum of a rock. *J Geophys Res: Solid Earth.* 1979;84(B13):7533–7543. <http://dx.doi.org/10.1029/JB084iB13p07533>.
64. Kuster GT, Toksöz MN. Velocity and attenuation of seismic waves in two-phase media: Part I, Theoretical formulations. *Geophysics.* 1974;39(5):587–606. <http://dx.doi.org/10.1190/1.1440450>.
65. Berryman JG. Long-wavelength propagation in composite elastic media II. Ellipsoidal inclusions. *J Acoust Soc Am.* 1980;68(6):1820–1831. <http://dx.doi.org/10.1121/1.385172>.
66. Norris AN. A differential scheme for the effective moduli of composites. *Mech Mater.* 1985;4(1):1–16. [http://dx.doi.org/10.1016/0167-6636\(85\)90002-X](http://dx.doi.org/10.1016/0167-6636(85)90002-X).
67. Blaber J, Adair B, Antoniou A. Ncorr: Open-source 2D digital image correlation matlab software. *Exp Mech.* 2015;55(6):1105–1122. <http://dx.doi.org/10.1007/s11340-015-0009-1>.
68. Moradian O, Wu R, Li Y, Leith K, Loew S. Acoustic emission and digital image correlation for damage evolution in brittle rocks under time-dependent tensile loading. *IOP Conf Ser: Earth Environ Sci.* 2021;833(1):12090. <http://dx.doi.org/10.1088/1755-1315/833/1/012090>.
69. Birch F. The velocity of compressional waves in rocks to 10 kilobars: 1.. *J Geophys Res (1896-1977).* 1960;65(4):1083–1102.
70. ASTM D-18. Standard test method for laboratory determination of pulse velocities and ultrasonic elastic constants of rock. In: *Annual Book of ASTM Standards*. ASTM International; 2008:356–363.
71. Aydin A. Upgraded ISRM suggested method for determining sound velocity by ultrasonic pulse transmission technique. In: *The ISRM Suggested Methods for Rock Characterization, Testing and Monitoring: 2007-2014*. Cham: Springer International Publishing; 2015:95–99.
72. Selvadurai PA, Wu R, Bianchi P, et al. A methodology for reconstructing source properties of a conical piezoelectric actuator using array-based methods. *J Nondestruct Eval.* 2022;41(1):23.
73. Wu R, Selvadurai PA, Chen C, Moradian O. Revisiting piezoelectric sensor calibration methods using elastodynamic body waves. *J Nondestruct Eval.* 2021;40(3):68.
74. Wu R, Selvadurai PA, Chen CJ, Moradian O. A FEM-based methodology to acquire broadband empirical green's functions to understand characterization tests of acoustic emission sensors. In: *54th US Rock Mechanics/Geomechanics Symposium*. OnePetro; 2020.
75. Eitzen DG, Wadley HNG. Acoustic emission: Establishing the fundamentals. *J Res Natl Bur Stand.* 1984;89(1):75–100.
76. Glaser SD, Weiss GG, Johnson LR. Body waves recorded inside an elastic half-space by an embedded, wideband velocity sensor. *J Acoust Soc Am.* 1998;104(3):1404–1412.
77. Kurz JH, Grosse CU, Reinhardt HW. Strategies for reliable automatic onset time picking of acoustic emissions and of ultrasound signals in concrete. *Ultrasonics.* 2005;43(7):538–546. <http://dx.doi.org/10.1016/J.ULTRAS.2004.12.005>.
78. Spetzler J, Snieder R. The Fresnel volume and transmitted waves. *Geophysics.* 2004;69(3):653–663. <http://dx.doi.org/10.1190/1.1759451>.
79. Bracewell RN. *The Fourier Transform and Its Applications*, vol. 31999. McGraw-Hill New York; 1986.
80. Bertschi R. AE-Amp Manual EN. In: *Elsys AG. Tech. rep.; Mellingerstrasse 12, CH-5443 Niederrohrdorf*. 2018:1–20. <https://www.elsys-instruments.com/en/products/ae-amp-preamplifier.php>.

81. Zemanek J, Rudnick I. Attenuation and dispersion of elastic waves in a cylindrical bar. *J Acoust Soc Am*. 1961;33(10):1283–1288. <http://dx.doi.org/10.1121/1.1908417>.
82. Johnson DL, Koplik J, Dashen R. Theory of dynamic permeability and tortuosity in fluid-saturated porous media. *J Fluid Mech*. 1987;176(-1):379. <http://dx.doi.org/10.1017/S0022112087000727>.
83. Prass J, Mütter D, Fratzl P, Paris O. Capillarity-driven deformation of ordered nanoporous silica. *Appl Phys Lett*. 2009;95(8):83121. <http://dx.doi.org/10.1063/1.3213564>.
84. David C, Barnes C, Desrues M, Pimienta L, Sarout J, Dautriat J. Ultrasonic monitoring of spontaneous imbibition experiments: Acoustic signature of fluid migration. *J Geophys Res: Solid Earth*. 2017;122(7):4931–4947. <http://dx.doi.org/10.1002/2016JB013804>.
85. Kovalyshen Y. Comment on “Ultrasonic monitoring of spontaneous imbibition experiments: precursory moisture diffusion effects ahead of water front” by David et al. (2017). *J Geophys Res: Solid Earth*. 2018;123(8):6607–6609. <http://dx.doi.org/10.1029/2018JB016040>.
86. Knott CG. Reflexion and refraction of elastic waves, with seismological applications. London, Edinburgh, Dublin Philos Mag J Sci. 1899;48(290):64–97.
87. Zoeppritz K. On the reflection and propagation of seismic waves. *Gottinger Nachrichten*. 1919;1(5):66–84.
88. David C, Barnes C, Sarout J, Dautriat J, Pimienta L. Reply to Comment by Y. Kovalyshen on “Ultrasonic monitoring of spontaneous imbibition experiments: Precursory moisture diffusion effects ahead of water front”. *J Geophys Res: Solid Earth*. 2018;123(8):6610–6615. <http://dx.doi.org/10.1029/2018JB016133>.
89. Taylor J. *Introduction To Error Analysis, the Study of Uncertainties in Physical Measurements*. University Science Books; 1997.
90. Salazar Vásquez A, Rabaiotti C, Germanovich LN, Puzrin AM. Distributed fiber optics measurements of rock deformation and failure in triaxial tests. *J Geophys Res: Solid Earth*. 2022;127(8):e2022JB023997. <http://dx.doi.org/10.1029/2022JB023997>, URL <https://agupubs.onlinelibrary.wiley.com/doi/abs/10.1029/2022JB023997>.
91. Gurevich B, Makarynska D, Pervukhina M. Ultrasonic moduli for fluid-saturated rocks: Mavko-Jizba relations rederived and generalized. *Geophysics*. 2009;74(4):N25–N30. <http://dx.doi.org/10.1190/1.3123802>.